Electronic Supplementary Material (ESI) for Inorganic Chemistry Frontiers.
This journal is © the Partner Organisations 2023

Supplementary Information

From Unprecedented 2,2'-Bisimidazole-Bridged Rare Earth Organometallics to Magnetic Hysteresis in the Dysprosium Congener

Florian Benner and Selvan Demir*

Department of Chemistry, Michigan State University, 578 S Shaw Lane, East Lansing, Michigan 48824, USA

*Correspondence to: sdemir@chemistry.msu.edu (S.D.)

Inorg. Chem. Front.

Table of Contents

1. Experimental Section

All manipulations were performed under inert conditions using either standard Schlenk techniques or nitrogen-filled glovebox. House nitrogen was purified through a MBraun HP-500-MO-OX gas purifier. Toluene, ^{n}hexane and ^{n}pentane were purified by refluxing over potassium using benzophenone as an indicator and distilled prior to use. THF was refluxed over potassium, distilled and subsequently refluxed over NaK and distilled a second time prior to use.
The chemicals pentamethylcyclopentadiene (Cp*H), allylmagnesium chloride (2.0 M in THF), ^{n}BuLi (2.5 M in hexane), anhydrous $RECl_3$ (Ln = Y, Gd, Dy) were purchased from Sigma Aldrich. H_2bim was purchased from TCI chemicals and dried in vacuum for 24 h prior to use. $Cp^*_2Ln(BPh_4)$[1] and Li_2Bim,[2] were synthesized according to literature procedures.

1.1 Synthesis of $[(Cp^*_2RE)_2(\mu\text{-bim})]$, 1-3

The rare earth metal tetraphenylborate complexes $Cp^*_2RE(BPh_4)$ (RE = Y, Gd, Dy) (2 equiv.) were dissolved in THF at 25 °C to give a pale yellow colored solution to which the dissolved dilithium bisimidazole Li_2bim (1 equiv.) in THF was added dropwise. The color gradually faded over the course of ~15 min to yield a colorless solution. After stirring for 3 h, the mixture was evaporated to dryness to afford an off-white solid which was triturated with ^{n}hexane and subsequently dried. The resulting off-white solid was extracted twice with toluene and the colorless insoluble solid was removed through filtration. The colorless filtrate (toluene solution) was concentrated and stored at –30 °C. Over the course of three days, crystals of **1**, **2** and **3**, respectively, suitable for single-crystal X-ray diffraction analysis were obtained. **1**, **2** and **3** are stable up to 60 °C. This was probed by heating the compounds in toluene at that temperature for a few hours which did not lead to decomposition.

$[(Cp^*_2Y)_2(\mu\text{-bim})]$, 1

Used masses: $Cp^*_2Y(BPh_4)$: 0.120 g (0.177 mmol), Li_2bim: 0.0387 g (0.0880 mmol). Crystalline yield of **1**: 0.0269 g (colorless block-shaped crystals, 0.0269 mmol, 31%). ^{1}H NMR (benzene-d_6, 500 MHz) δ (ppm) = 6.73 (s, 4H, bim-H), 1.84 (s, 60H, Cp*-Me). ^{13}C NMR (benzene-d_6, 125 MHz) δ (ppm) = 147.09 (s, C2), 126.52 (s, C4/C5), 117.75 (s, C-Cp*), 11.12 (s, C-Me-Cp*). IR (ATR, cm^{-1}): 3101 (vw), 2970 (w), 2900 (m), 2855 (m), 2721 (w), 1688 (w), 1453 (m), 1439 (m), 1401 (vs), 1382 (s), 1305 (m), 1271 (w), 1126 (vs), 1092 (m), 1021 (w), 947 (m), 764 (s), 708 (w). Anal. Calcd for $C_{46}H_{64}N_4Y_2$ (%): C, 64.93; H, 7.58; N, 6.58. Found: C, 64.72; H, 7.51; N, 6.61.

$[(Cp^*_2Gd)_2(\mu\text{-bim})]$, 2

Used masses: $Cp^*_2Gd(BPh_4)$: 0.127 g (0.170 mmol), Li_2bim: 0.0417 g (0.0847 mmol). Crystalline yield of **2**: 0.0442 g (colorless block-shaped crystals, 0.0448 mmol, 52%). ^{1}H NMR (benzene-d_6, 500 MHz) δ [ppm] = −0.14 (br s, 15H), −25.09 (br s, 60H). ^{1}H NMR signals are significantly broadened due to the presence of paramagnetic Gd^{III} ions, preventing an accurate assignment of the signals. Compound **2** did not display any signals in ^{13}C NMR spectroscopy. IR (ATR, cm^{-1}): 3101 (vw), 2974 (w), 2900 (s), 2855 (s), 2728 (w), 1453 (m), 1437 (m), 1401 (vs), 1382 (s), 1305 (m), 1271 (w), 1126 (vs), 1092 (m), 1017 (m), 947 (m), 760 (s), 708 (w). Anal. Calcd for $C_{46}H_{64}N_4Gd_2$ (%): C, 55.95; H, 6.53; N, 5.67. Found: C, 56.04; H, 6.88, N: 6.18.

$[(Cp^*_2Dy)_2(\mu\text{-bim})]$, 3

Used masses: $Cp^*_2Dy(BPh_4)$: 0.117 g (0.156 mmol), Li_2bim: 0.0387 g (0.0786 mmol). Crystalline yield of **3**: 0.0408 g (pale yellow block-shaped crystals, 0.0409 mmol, 52%). ^{1}H NMR (benzene-d_6, 500 MHz) δ [ppm] = −1.99 (br s, 15H), −15.25 (br s, 60H). ^{1}H NMR signals are

significantly broadened due to presence of paramagnetic Dy^{III} ions, preventing an accurate assignment of the signals. Compound **3** did not display any signals in ^{13}C-NMR spectroscopy. IR (ATR, cm^{-1}): 3105 (vw), 2971 (w), 2900 (s), 2859 (s), 2721 (w), 1669 (vw), 1450 (m), 1402 (vs), 1379 (s), 1305 (m), 1271 (w), 1126 (vs), 1092 (s), 1018 (m), 947 (s), 764 (vs), 708 (w). Anal. Calcd for $C_{46}H_{64}N_4Dy_2$ (%): C, 55.36; H, 6.46; N, 5.61. Found: C, 55.36; H, 6.31; N, 5.66.

1.2 Analysis

NMR Spectroscopy

NMR spectra were recorded on a 500 MHz Agilent DirectDrive2 500 at Michigan State University and calibrated to the residual solvent signals (C_6D_6: δ_H = 7.16 ppm, δ_C = 128.4 ppm). Signal multiplicities are abbreviated as: s (singlet), d (doublet), m (multiplet), br (broad). Air sensitive samples were prepared in a nitrogen-filled glovebox using Young NMR tubes. NMR solvent (C_6D_6) was dried by refluxing over potassium and subsequent distillation. Distillated solvent was stored over activated mole sieves (4 Å).

IR Spectroscopy

IR spectra were recorded with a Cary 630 ATR IR spectrometer from Agilent Technologies in an argon-filled glovebox.

UV/Vis spectroscopy

UV-vis spectra were collected with a Agilent Cary 60 spectrometer UV-Vis spectrometer at ambient temperature from 220 to 1100 nm. Samples were prepared in a dry argon-filled glove box and measured in a 1 cm quartz cuvette, outfitted with a Teflon screw cap. The spectra were baseline corrected from a sample of dry and filtered THF.

Magnetic Susceptibility Measurements

Magnetic measurements were conducted with a Quantum Design MPMPS3 SQUID magnetometer. Crystalline materials of **2** and **3** were rinsed with cold THF and dried under vacuum for 1 h prior to sample preparation. Molten eicosane was added at 60 °C to the sample to immobilize the crystallites and to ensure good thermal contact between sample and the bath. The samples were sealed airtight and transferred to the SQUID magnetometer. All data were corrected for diamagnetic contributions from the eicosane and core diamagnetism estimated using Pascal's constants.[3]

Elemental Analysis

Elemental analysis was obtained on a PerkinElmer 2400 Series II CHNS/O analyzer at Michigan State University. In a nitrogen-filled glovebox, solid samples (~1 – 3 mg) were weighed into tin sample holders and folded multiple times to ensure proper sealing from surrounding atmosphere. Samples were taken to the instrument in airtight vials.

X-ray Crystallography

Suitable single crystals for X-ray structure determination were selected from the mother liquor under an inert gas atmosphere and transferred in protective perfluoro polyether oil on a microscope slide. The selected and mounted crystals were transferred to the cold gas stream on the diffractometer.

Data of compound **1** were collected using a Bruker Apex-II CCD (charge coupled device) based diffractometer equipped with an Oxford Cryostream low-temperature apparatus operating at

173 K. Data were measured using omega and phi scans of 1.0° per frame for 30 s. The total number of images was based on results from the program COSMO[4] where redundancy was expected to be 4.0 and completeness of 100% out to 0.83 Å. Cell parameters were retrieved using APEX II software[5] and refined using SAINT on all observed reflections. Data reduction was performed using the SAINT software[6] which corrects for Lp. Scaling and absorption corrections were applied using SADABS[7] multi-scan technique, supplied by Dr. George Sheldrick. Using Olex2,[8] the structure was solved with the ShelXT[9] structure solution program using Intrinsic Phasing and refined by least squares method on F^2, SHELXL-97,[10] which are incorporated in SHELXTL-PC V 6.10.[11] All non-hydrogen atoms are refined anisotropically. Hydrogens were calculated by geometrical methods and refined as a riding model. All drawings are done at 50% ellipsoids.

Data of compounds **2** and **3** were collected on a XtaLAB Synergy Dualflex HyPix four-circle diffractometer, equipped with a HyPix Hybrid Pixel Array Detector. The crystal was kept at 100.00(10) K during data collection. Data were measured using CuK_α radiation. The maximum resolution that was achieved was Θ = 71.296° (0.81 Å). The CrysAlisPro software package[12] was used to retrieve and refine the cell parameters, as well as for data reduction. Correction for absorption effects was done using a numerical correction based on gaussian integration over a multifaceted crystal model and an empirical correction using spherical harmonics, implemented in SCALE3 ABSPACK[13] scaling algorithm (spherical harmonics and frame scaling). Using Olex2,[8] the structure was solved with the ShelXT[9] structure solution program using intrinsic phasing and refined with version 2018/3 of ShelXL-2018/3[10] using Least Squares minimization. All non-hydrogen atoms were refined anisotropically. Hydrogen atom positions were calculated geometrically and refined using the riding model. Hydrogen atom positions were calculated geometrically and refined using the riding model.

Computational Studies

All calculations were carried out using the Orca program suite, version 5.0.3.[14] Geometry optimizations of **1** and $[(Cp^*_2Y)_2(\mu\text{-Bbim})]$ were first carried on the uncontracted complex starting from the crystal coordinates using the TPSSh hybrid functional[15,16] with the def2-SVP[17] basis set on all atoms, ECP-28 core potentials on yttrium atoms,[18] and the def2/J auxiliary basis[19] set with standard grid settings accompanied by the slowconv keyword. These preoptimized coordinates were further refined through the inclusion of def-TZVP[17] basis sets on the Y atoms and all atoms belonging to the bridging Bim ligand. The D3BJ dispersion correction[20,21] and the RijCosX approximation[22,23] were used throughout. Graphical representations of the orbitals were generated using the VMD software.[15]

TDDFT calculations were carried out on the TZVP-optimized coordinates on 75 excited states under consideration of the SMD solvent model[24] for THF. The calculated transitions are listed in Table S4, Table S5 and Table S6.

The energies for $\mathbf{1}^+$, $\mathbf{1}^-$, $[(Cp^*_2Y)_2(\mu\text{-bim})]^+$ and $[(Cp^*_2Y)_2(\mu\text{-bim})]^-$ were obtained starting from the TZVP-optimized coordinates of the neutral complexes and subsequent reoptimization with the charges and multiplicities adjusted to $^{+1}/2$ and $^{-1}/2$ at the uTPSSh/def2-SVP(Cp*)/def2-TZVP(Y,ligand)/D3BJ level.

2 ^{1}H NMR Spectroscopy

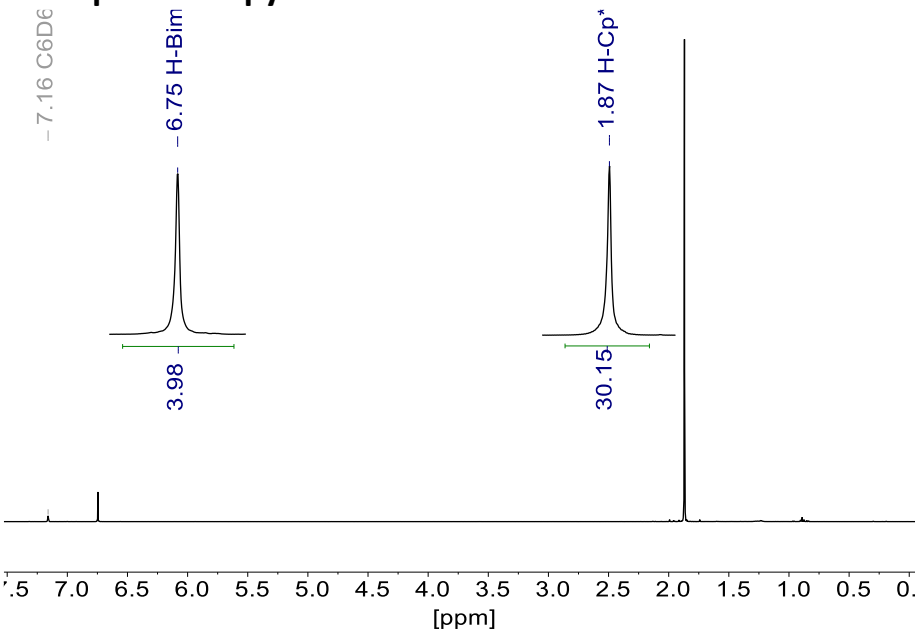

Figure S1. ^{1}H NMR spectrum of [(Cp*$_2$Y)$_2$(μ-bim)], **1** (500 MHz, 25 °C, benzene-d_6).

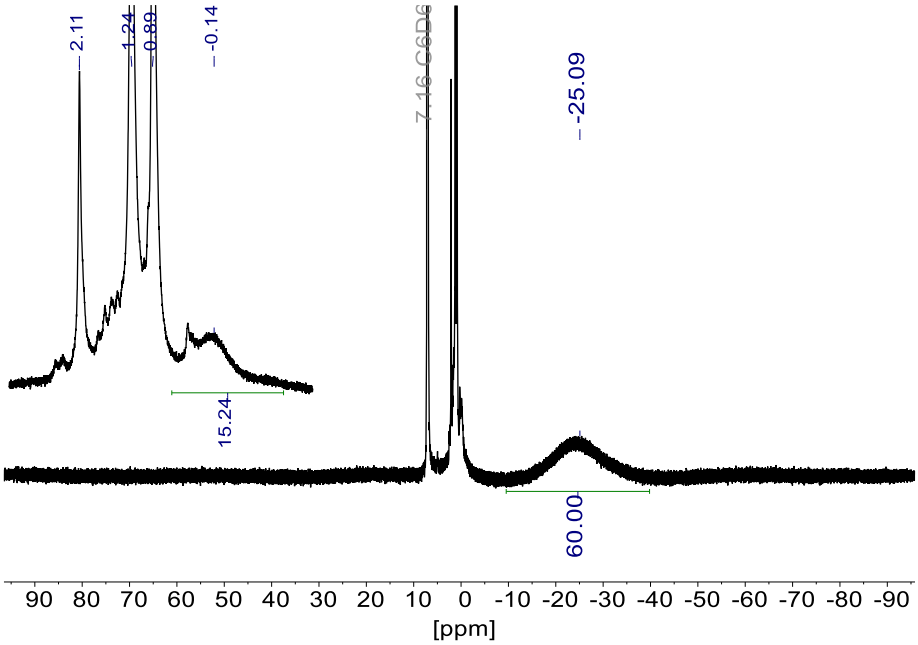

Figure S2. ^{1}H NMR spectrum of [(Cp*$_2$Gd)$_2$(μ-bim)], **2** (500 MHz, 25 °C, benzene-d_6).

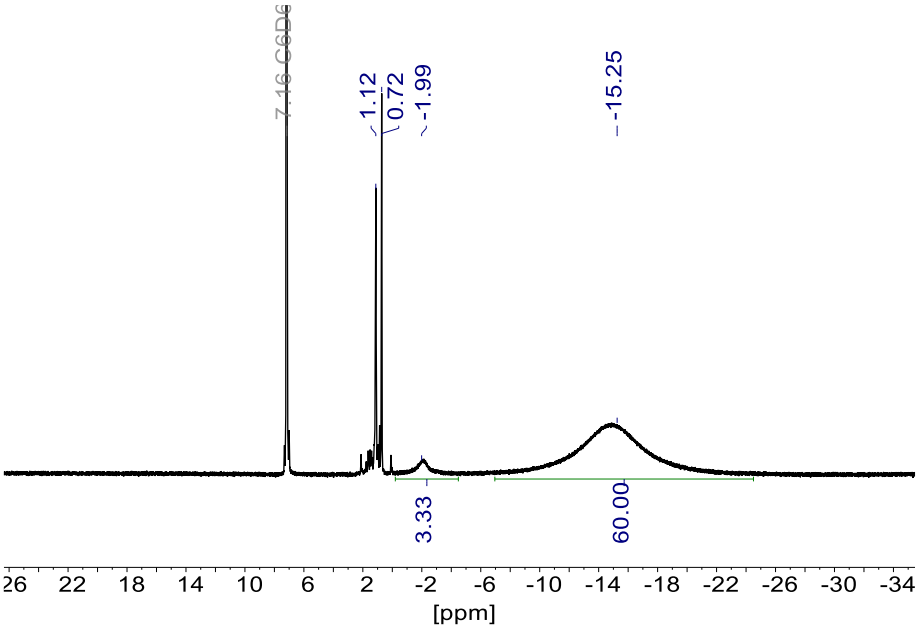

Figure S3. ^{1}H NMR spectrum of [(Cp*$_2$Dy)$_2$(μ-bim)], **3** (500 MHz, 25 °C, benzene-d_6).

3 ^{13}C NMR Spectroscopy

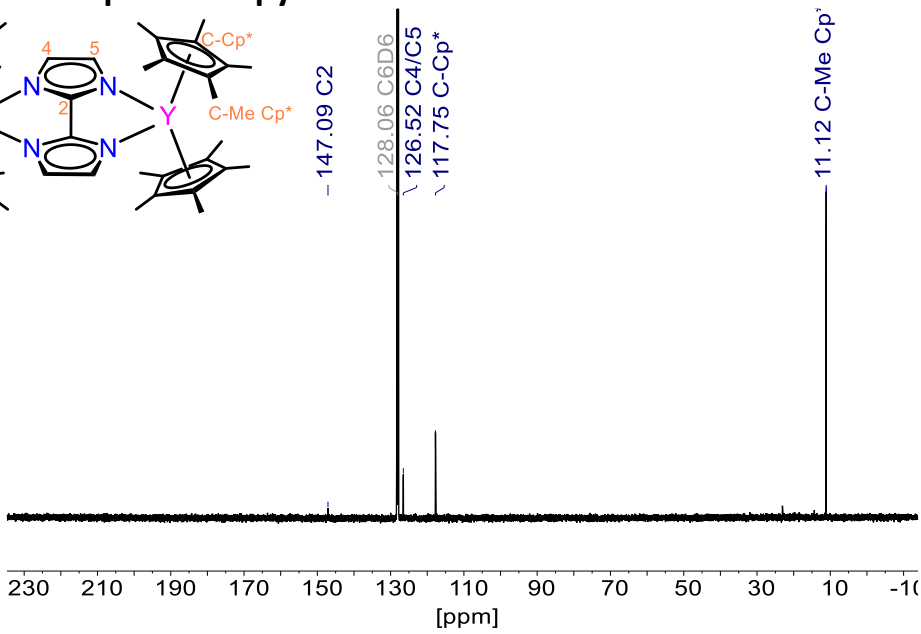

Figure S4. ^{13}C NMR spectrum of [(Cp*$_2$Y)$_2$(μ-bim)], **1** (125 MHz, 25 °C, benzene-d_6).

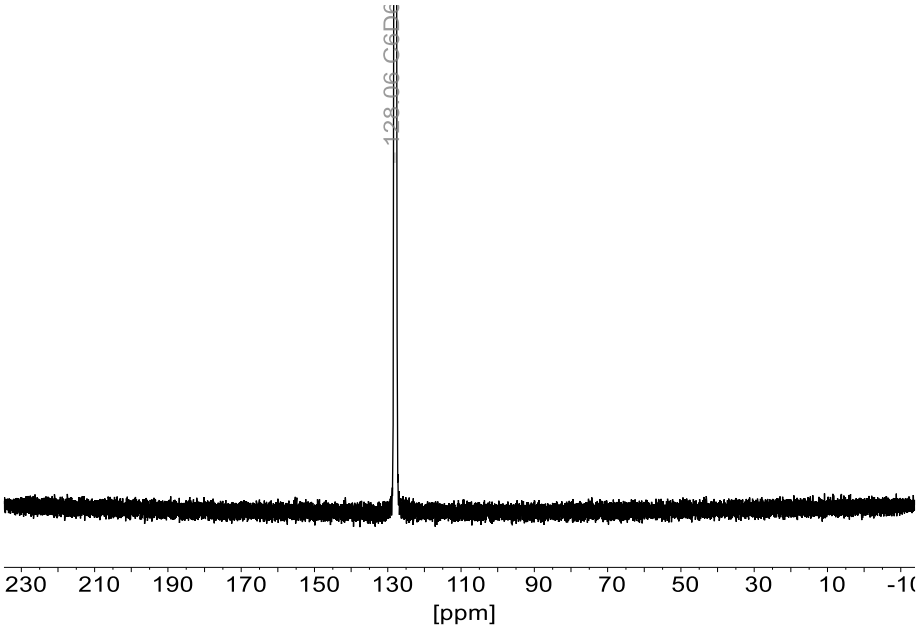

Figure S5. ^{13}C NMR spectrum of [(Cp*$_2$Gd)$_2$(μ-bim)], **2** (125 MHz, 25 °C, benzene-d_6).

4 IR Spectroscopy

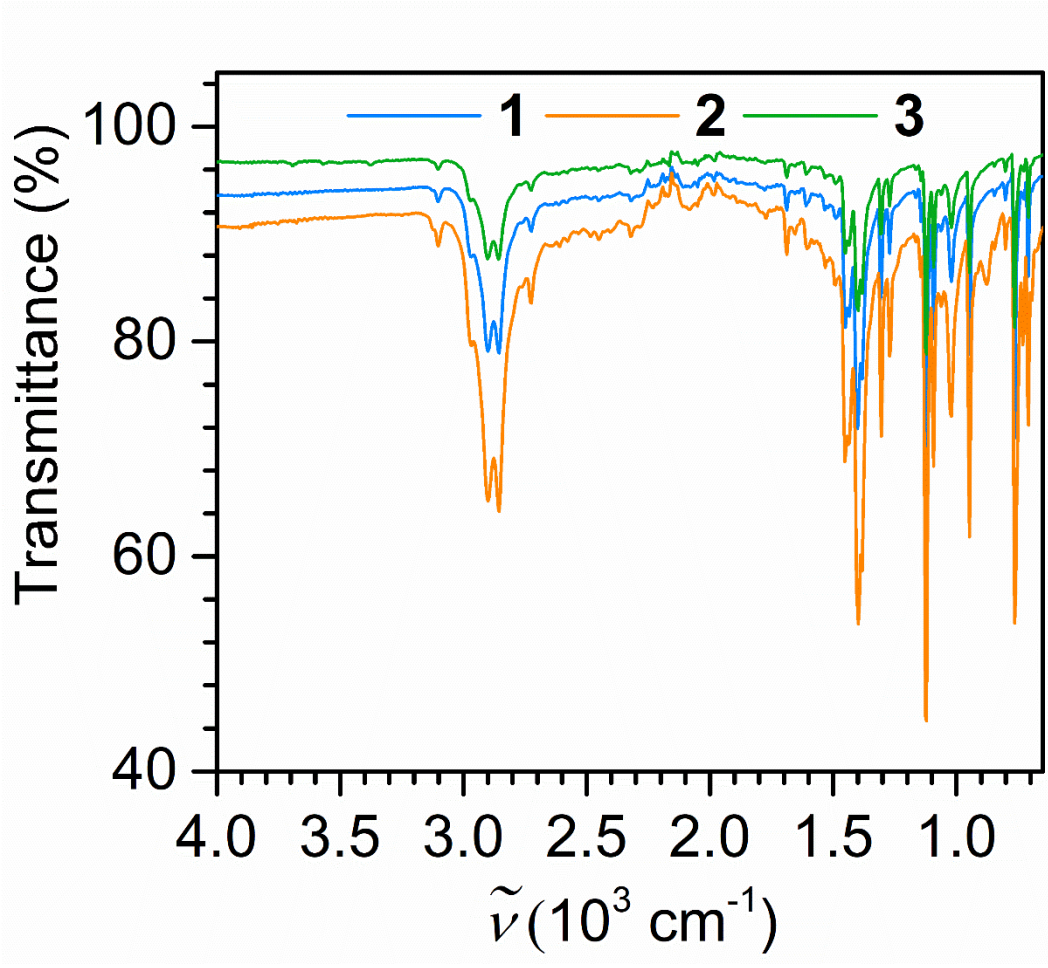

Figure S6. ATR IR spectrum of [(Cp*$_2$RE)$_2$(μ-bim)] (RE = Y (**1**), Gd (**2**), Dy (**3**)).

5 Crystallographic Data and Structural Refinements

Table S1. Crystallographic Data and Structural Refinement of [(Cp*$_2$Y)$_2$(μ-bim)], **1**.

Empirical formula	$C_{46}H_{64}N_4Y_2$
CCDC	2251266
Formula weight	850.83
Temperature/K	173(1)
Crystal system	monoclinic
Space group	$P2_1/c$
a [Å]	11.9961(16)
b [Å]	12.0094(16)
c [Å]	15.842(2)
α [°]	90
β [°]	110.929(2)
γ [°]	90
Volume [Å^3]	2131.7(5)
Z	2
ρ_{calc} [g/cm^3]	1.326
μ [mm^{-1}]	2.744
F(000)	892.0
Crystal size [mm^3]	0.205 × 0.155 × 0.104
Radiation	MoK$_\alpha$ (λ = 0.71073)
2Θ range for data collection [°]	3.634 to 51.526
Index ranges	-14 ≤ h ≤ 14, -14 ≤ k ≤ 14, -19 ≤ l ≤ 19
Reflections collected	17340
Independent reflections	4087 [R_{int} = 0.1007, R_s = 0.0915]
Data/restraints/parameters	4087/0/245
Goodness-of-fit on F^2	1.004
Final R indexes [I > = 2 σ (I)]	R_1 = 0.0497, wR_2 = 0.0968
Final R indexes [all data]	R_1 = 0.0963, wR_2 = 0.1158
Largest diff. peak/hole [e Å^{-3}]	0.96/-0.48

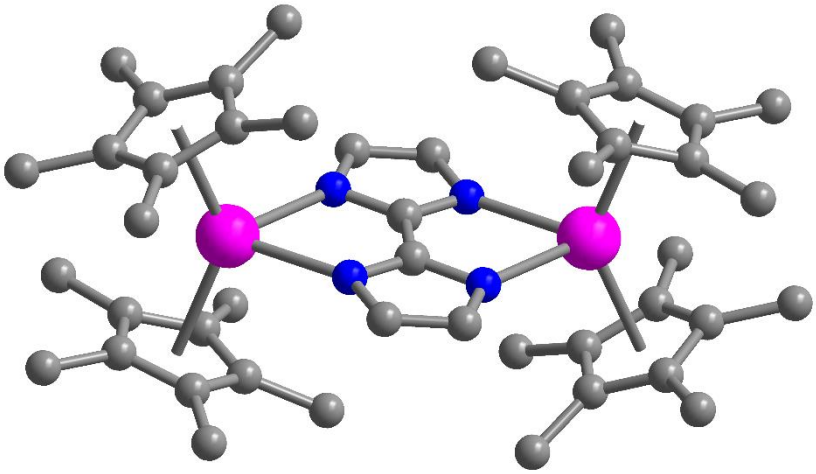

Figure S7. Structure of **1**. Pink, blue, and grey spheres represent Y, N and C atoms, respectively. H atoms are omitted for clarity.

Table S2. Crystallographic Data and Structural Refinement of [(Cp*$_2$Gd)$_2$(μ-bim)], **2**.

Empirical formula	$C_{46}H_{64}Gd_2N_4$
CCDC	2251267
Formula weight	987.51
Temperature/K	100.00(10)
Crystal system	monoclinic
Space group	$P2_1/c$
a [Å]	11.9387(4)
b [Å]	12.0097(3)
c [Å]	15.8069(5)
α [°]	90
β [°]	110.384(4)
γ [°]	90
Volume [Å^3]	2124.47(12)
Z	2
ρ_{calc} [g/cm^3]	1.544
μ [mm^{-1}]	20.228
F(000)	992.0
Crystal size [mm^3]	0.136 × 0.056 × 0.046
Radiation	Cu K_α (λ = 1.54184)
2Θ range for data collection [°]	7.9 to 142.592
Index ranges	$-14 \le h \le 14$, $-14 \le k \le 14$, $-19 \le l \le 12$
Reflections collected	9939
Independent reflections	3950 [R_{int} = 0.0311, R_s = 0.0363]
Data/restraints/parameters	3950/0/245
Goodness-of-fit on F^2	1.042
Final R indexes [$I >= 2\sigma(I)$]	R_1 = 0.0282, wR_2 = 0.0697
Final R indexes [all data]	R_1 = 0.0329, wR_2 = 0.0719
Largest diff. peak/hole [e Å^{-3}]	0.55/-0.83

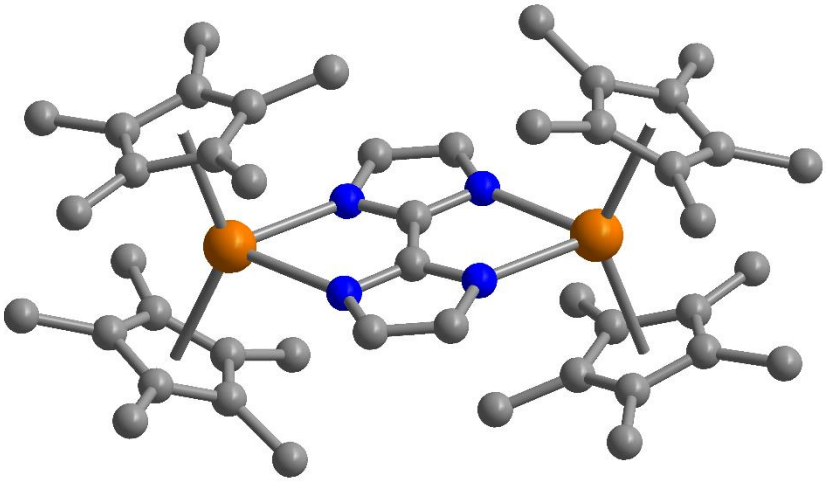

Figure S8. Structure of **2**. Orange, blue, and grey spheres represent Gd, N and C atoms, respectively. H atoms are omitted for clarity.

Table S3. Crystallographic Data and Structural Refinement of [(Cp*$_2$Dy)$_2$(μ-bim)], **3**.

Empirical formula	$C_{46}H_{64}Dy_2N_4$
CCDC	2251271
Formula weight	998.01
Temperature/K	100.00(10)
Crystal system	monoclinic
Space group	$P2_1/c$
a [Å]	11.9239(3)
b [Å]	11.9642(2)
c [Å]	15.7798(4)
α [°]	90
β [°]	110.597(3)
γ [°]	90
Volume [Å^3]	2107.25(9)
Z	2
ρ_{calc} [g/cm^3]	1.573
μ [mm^{-1}]	19.008
F(000)	1000.0
Crystal size [mm^3]	0.083 × 0.055 × 0.053
Radiation	CuK$_\alpha$ (λ = 1.54184)
2Θ range for data collection [°]	7.92 to 142.618
Index ranges	$-9 \le h \le 14$, $-14 \le k \le 12$, $-19 \le l \le 18$
Reflections collected	10758
Independent reflections	3957 [R_{int} = 0.0275, R_{sigma} = 0.0314]
Data/restraints/parameters	3957/0/245
Goodness-of-fit on F^2	1.036
Final R indexes [$I >= 2\sigma(I)$]	R_1 = 0.0225, wR_2 = 0.0552
Final R indexes [all data]	R_1 = 0.0252, wR_2 = 0.0563
Largest diff. peak/hole [e Å^{-3}]	0.47/-0.46

6 UV/Vis Spectroscopy

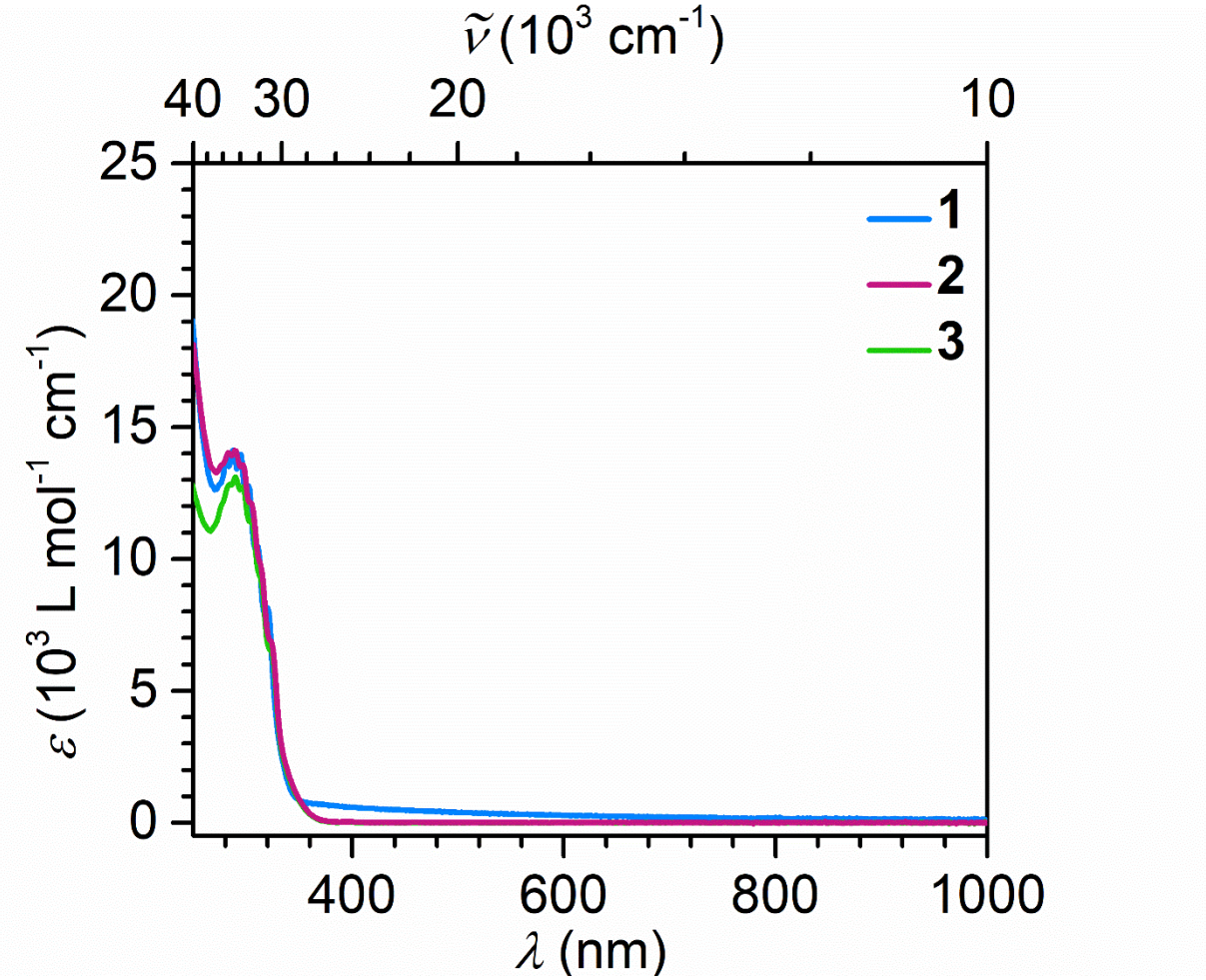

Figure S9. Full experimental UV/Vis spectra of [(Cp*$_2$RE)$_2$(μ-bim)] (Ln = Y (**1**), Gd (**2**), Dy (**3**)), recorded at room temperature in THF solution. Concentrations: 22.38 μmol/L (**1**), 28.65 μmol/L, (**2**) 24.60 μmol/L (**3**).

7 TDDFT calculations

Table S4. TDDFT-calculated transitions for [(Cp*$_2$Y)$_2$(μ-bim)], obtained on the optimized crystal coordinates on the def2-SVP(Cp*)/def2-TZVP(Y,bim) level of theory using the TPSSh functional with dispersion correction D3BJ and implicit solvent model SMD for THF. The cutoff for printing was set to oscillator strengths < 0.035. Bold occupied orbitals represent predominantly bim-centered orbitals. The calculated excitation energies were empirically red-shifted by 0.1 eV.

λ (nm)	**$\tilde{\nu}$ (cm^{-1})**	**Oscillator strength**	**Dominant Contributions (>20%)**		**Weight (%)**	**Assignment**
			Occupied	Virtual		
325.4	30730.9	0.035713377	192 (HOMO−2)	196 (HOMO+2)	22	Cp–Y → (bim)*
			193 (HOMO−1)	195 (LUMO)	21	Cp–Y+bim → (Y *d*)*
			194 (HOMO)	195 (LUMO)	35	bim → (Y *d*)*
321.3	31128.3	0.097164424	192 (HOMO−2)	**196** (HOMO+2)	33	Cp–Y → (bim)*
			193 (HOMO−1)	195 (LUMO)	37	Cp–Y+bim → (Y *d*)*
319.9	31255.2	0.059876332	191 (HOMO−3)	195 (LUMO)	90	Cp–Y → (Y *d*)*
317.7	31474.6	0.039981592	192 (HOMO−2)	**196** (HOMO+2)	20	Cp–Y → (bim)*
			194 (HOMO)	197 (HOMO+3)	48	bim → (Bim/Y *d*)*
309.3	32331.4	0.139254490	**193** (HOMO−1)	195 (LUMO)	32	Cp–Y+bim → (Y *d*)*
			194 (HOMO)	195 (LUMO)	39	bim → (Y *d*)*
299.3	33410.2	0.040590879	188 (HOMO−6)	195 (LUMO)	97	Cp–Y → (Y *d*)*
280.8	35616.1	0.174855759	186 (HOMO−8)	195 (LUMO)	83	Cp–Y → (Y *d*)*
254.3	39319.0	0.034470573	191 (HOMO−3)	198 (HOMO+4)	41	Cp–Y → (Cp–Y)*

249.4	40088.9	0.031857000	190 (HOMO−4)	199 (HOMO+5)	41	Cp–Y → (Cp–Y)*
			194 (HOMO)	202 (HOMO+8)	30	bim → (Cp*)*
248.1	40303.8	0.084185223	190 (HOMO−4)	200 (HOMO+6)	83	Cp–Y → (bim/Y *d*)*
245.7	40707.1	0.062638581	188 (HOMO−6)	198 (HOMO+4)	38	Cp–Y → (Cp–Y)*
			189 (HOMO−5)	198 (HOMO+4)	32	Cp–Y → (Cp–Y)*
239.1	41818.0	0.037383398	187 (HOMO−7)	199 (HOMO+5)	34	Cp–Y → (Cp–Y)*
			187 (HOMO−7)	200 (HOMO+6)	24	Cp–Y → (bim/Y *d*)*
238.1	42002.6	0.072911097	187 (HOMO−7)	199 (HOMO+5)	20	Cp–Y → (Cp–Y)*
			187 (HOMO−7)	200 (HOMO+6)	62	Cp–Y (bim/Y *d*)*
236.8	42235.4	0.048761718	187 (HOMO−7)	201 (HOMO+7)	52	Cp–Y (bim/Y *d*)*
235.6	42453.5	0.066205304	**194** (HOMO)	204 (HOMO+10)	35	bim → (Cp*)*
			194 (HOMO)	205 (HOMO+11)	43	bim (bim/Y *d*)*
234.3	42677.3	0.118377473	**194** (HOMO)	204 (HOMO+10)	32	bim → (Cp*)*
			194 (HOMO)	205 (HOMO+11)	31	bim (bim/Y *d*)*
233.7	42787.3	0.074934817	186 (HOMO−8)	198 (HOMO+4)	71	Cp–Y → (Cp–Y)*

Table S5. TDDFT-calculated transitions of primarily bim-centered orbitals 193 and 194 into the bim-centered HOMO+2 (no. 196).

λ (nm)	**$\tilde{\nu}$ (cm^{-1})**	**Oscillator strength**	**Dominant Contributions (>20%)**		**Weight (%)**
			Occupied	Virtual	
329.2	30377.8	0.000000041	**194** (HOMO)	**196** (HOMO+2)	97
322.8	30975.4	0.000000072	192	195	52
			193	**196**	30
320.8	31169.4	0.000033090	192	195	34
			193	**196**	55

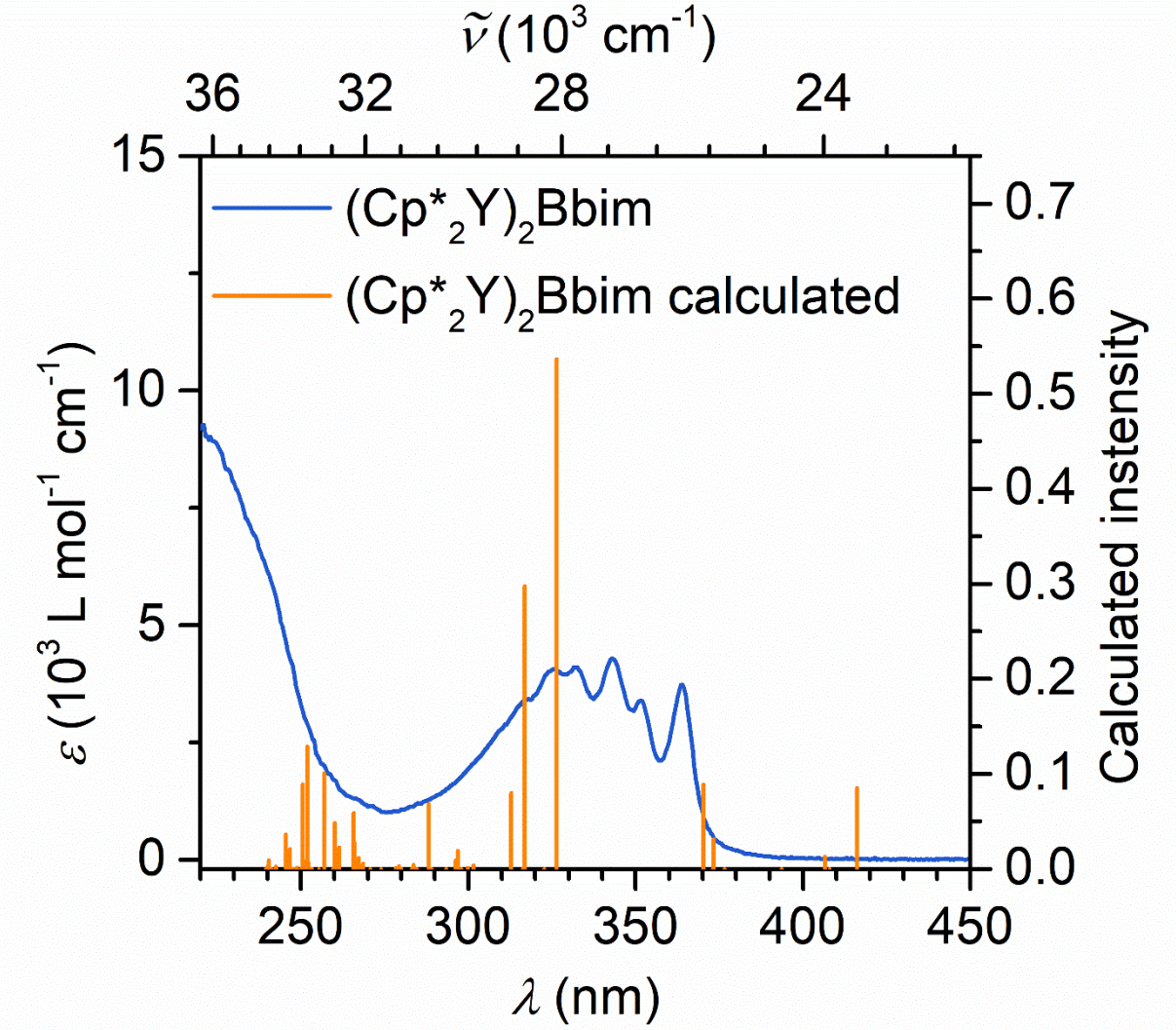

Figure S10. Overlay of experimental UV/Vis spectrum of [(Cp*$_2$Y)$_2$(μ-Bbim)] with TDDFT-calculated transitions obtained on the optimized crystal coordinates on the def2-SVP(Cp*)/def2-TZVP(Y,Bbim) level of theory using the TPSSh functional with dispersion correction D3BJ and implicit solvent model SMD for THF. The cutoff for printing was set to oscillator strengths < 0.035. Concentration experimental spectrum: 8.054 μmol/L in THF.

Table S6. TDDFT-calculated transitions for [(Cp*$_2$Y)$_2$(μ-bim)], obtained on the optimized crystal coordinates on the def2-SVP(Cp*)/def2-TZVP(Y,Bbim) level of theory using the TPSSh functional with dispersion correction D3BJ and implicit solvent model SMD for THF. The cutoff for printing was set to oscillator strengths < 0.035.

λ (nm)	**$\tilde{\nu}$ (cm^{-1})**	**Oscillator strength**	**Dominant Contributions (>20%)**		**Weight (%)**	**Assignment**
			Occupied	Virtual		
416.2	24025.2	0.085047282	220 (HOMO)	221 (LUMO)	97	Cp* → (Bbim)*
370.2	27014.7	0.088691397	213 (HOMO−7)	221 (LUMO)	38	Cp* → (Bbim)*
			215 (HOMO−5)	221 (LUMO)	39	Cp–Y → (Bbim)*
326.4	30635.5	0.536369304	212 (HOMO−8)	221 (LUMO)	79	(Bbim/Cp*-π) → (Bbim)*
316.9	31560.1	0.297657634	219 (HOMO−1)	222 (HOMO+2)	60	Cp* → (Y *d*)*
312.8	31970.5	0.080140535	217 (HOMO−3)	222 (HOMO+2)	41	Cp–Y → (Y *d*)*
			220 (HOMO)	223 (HOMO+3)	35	Cp* → (Y *d*)*
288.2	34702.5	0.068230043	210 (HOMO−10)	221 (LUMO)	89	BBim → (Bbim)*
265.8	37628.2	0.058887930	219 (HOMO−1)	225 (HOMO+5)	21	Cp* → (Bbim)*
			220 (HOMO)	226 (HOMO+6)	73	Cp* → (Bbim/Y *d*)*
260.1	38453.5	0.048365883	217 (HOMO−3)	225 (HOMO+5)	86	Cp–Y → (Bbim)*
257.0	38909.4	0.100793541	220 (HOMO)	227 (HOMO+7)	95	Cp* → (Cp–Y)*
251.9	39694.5	0.128660537	215 (HOMO−5)	225 (HOMO+5)	22	Cp–Y → (Bbim)*

			216 (HOMO−4)	**225** (HOMO+2)	68	Bbim → (Bbim)* π → π*
250.6	39902.3	0.089181109	214 (HOMO−6)	225 (HOMO+5)	83	Cp–Y → (Bbim)*
245.5	40731.5	0.036270645	213 (HOMO−7)	226 (HOMO+6)	21	Cp* → (Bbim/Y *d*)*
			219 (HOMO−6)	228 (HOMO+8)	61	Cp* → (Bbim)*

Table S7. Calculated energies for [(Cp*$_2$Y)$_2$(μ-bim)] (**1**) and [(Cp*$_2$Y)$_2$(μ-Bbim)].

	[(Cp*$_2$Y)$_2$(μ-bim)] (**1**)	[(Cp*$_2$Y)$_2$(μ-Bbim)]
E (α HOMO) (eV)	−4.9137	−4.9731
E (α LUMO) (eV)	−0.8182	−1.7275
Δ*E* (α) (eV)	4.0955	3.2456
E (β HOMO) (eV)	−4.9137	−4.9731
E (β LUMO) (eV)	−0.8182	−1.7275
Δ*E* (β) (eV)	4.0955	3.2456
E_{SP} neutral (H)	−2087.005933272414	−2394.470153749403
E_{SP} cation (H)	−2086.783102053347	−2394.249400167309
E_{SP} anion (H)	−2086.998378777322	−2394.493731685417

8 Cyclic voltammetry

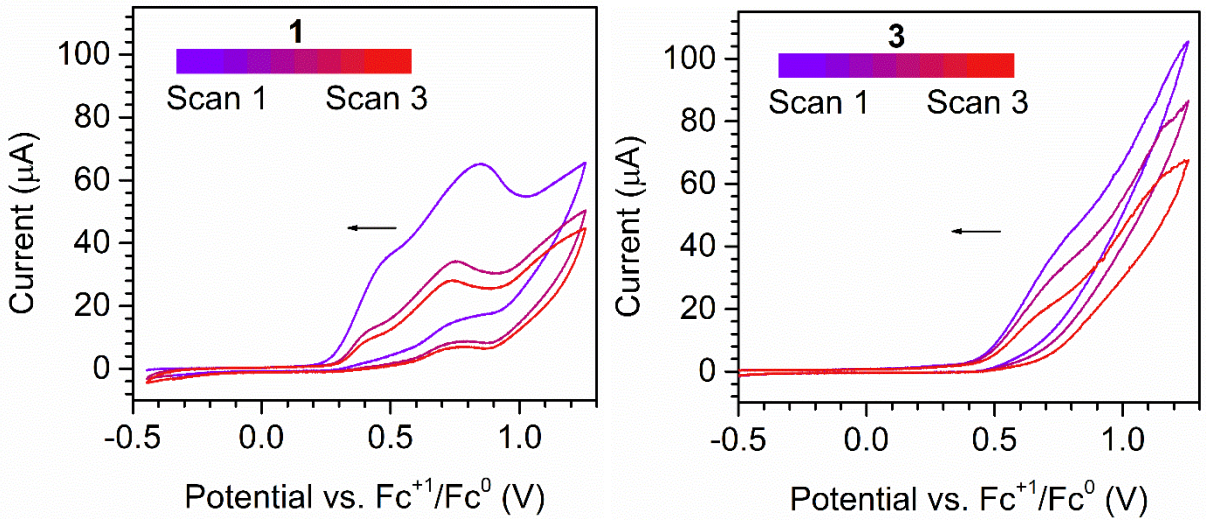

Figure S11. Cyclic voltammograms of **1** and **3**, recorded on a three-electrode setup comprising a glassy carbon working electrode, a Pt mesh counter electrode and a Ag wire reference electrode, using a 210 mmol/L concentration of (^{n}Bu$_4$N)(PF$_6$) supporting electrolyte in dichloromethane. The scans were externally referenced against the ferrocene/ferrocenium redox couple.

9 Magnetic measurements

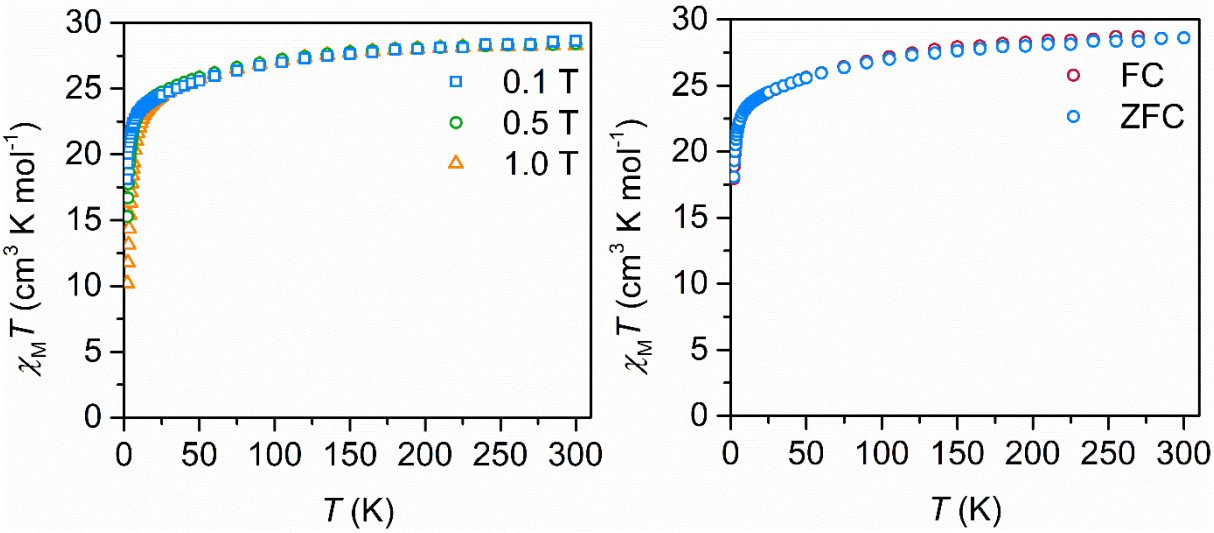

Figure S12. Variable-temperature dc susceptibility data of polycrystalline [(Cp*$_2$Dy)$_2$(μ-bim)] (**3**), collected under 0.1 T (blue squares), 0.5 T (green circles) and 1.0 T (orange triangles) applied dc fields (left). Superimposed zfc (blue circles) and fc (red circles) of **3**, recorded at 0.1 T (right).

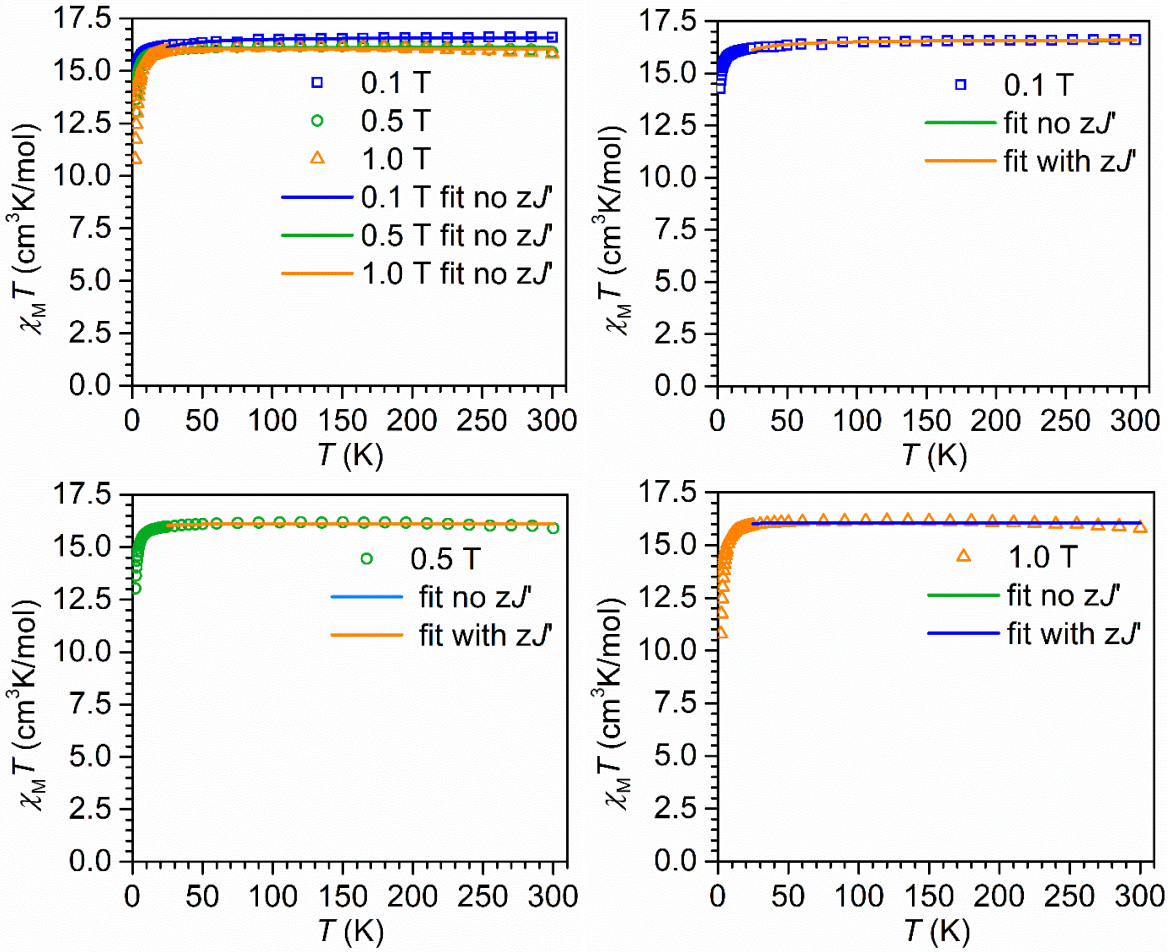

Figure S13. Variable-temperature dc susceptibility data of polycrystalline [(Cp*$_2$Gd)$_2$(μ-bim)] (**2**), collected under 0.1 T (blue squares), 0.5 T (green circles) and 1.0 T (orange triangles) applied dc fields (left). Solid lines represent fits considering exchange coupling *J* and the *g*-value with a constant intermolecular *zJ*' contribution of 0.075 cm^{-1} over 25 K. Fit values are given in Table S8. Variable-temperature dc susceptibility data of **2** collected at 0.1 T with fits including (green line) and excluding (orange line) *zJ*' contributions (top right). Variable-temperature dc susceptibility data of **2** collected at 0.5 T with fits including (blue line) and excluding (orange line) *zJ*' contributions (bottom left). Variable-temperature dc susceptibility data of **2** collected at 1.0 T with fits including (green line) and excluding (blue line) *zJ*' contributions (bottom left).

Table S8. Fit values for high temperature zfc dc curves (>25 K) of [(Cp*$_2$Gd)$_2$(μ-bim)] (**2**), recorded at 0.1 T, 0.5 T and 1.0 T, considering exchange coupling *J* and the *g*-value with and without intermolecular coupling *zJ*'.

Field (T)	*g*	*J* (cm^{-1})	*zJ*' (cm^{-1})	Residue
0.1	2.0543(5)	−0.045(2)	-	0.031
0.1	2.0541(6)	−0.074(2)	−0.0075	0.033
0.5	2.023(1)	−0.004(4)	-	0.12
0.5	2.023(1)	−0.035(4)	−0.0075	0.12
1.0	2.019(1)	0.002(5)	-	0.18
1.0	2.019(1)	−0.028(5)	−0.0075	0.18

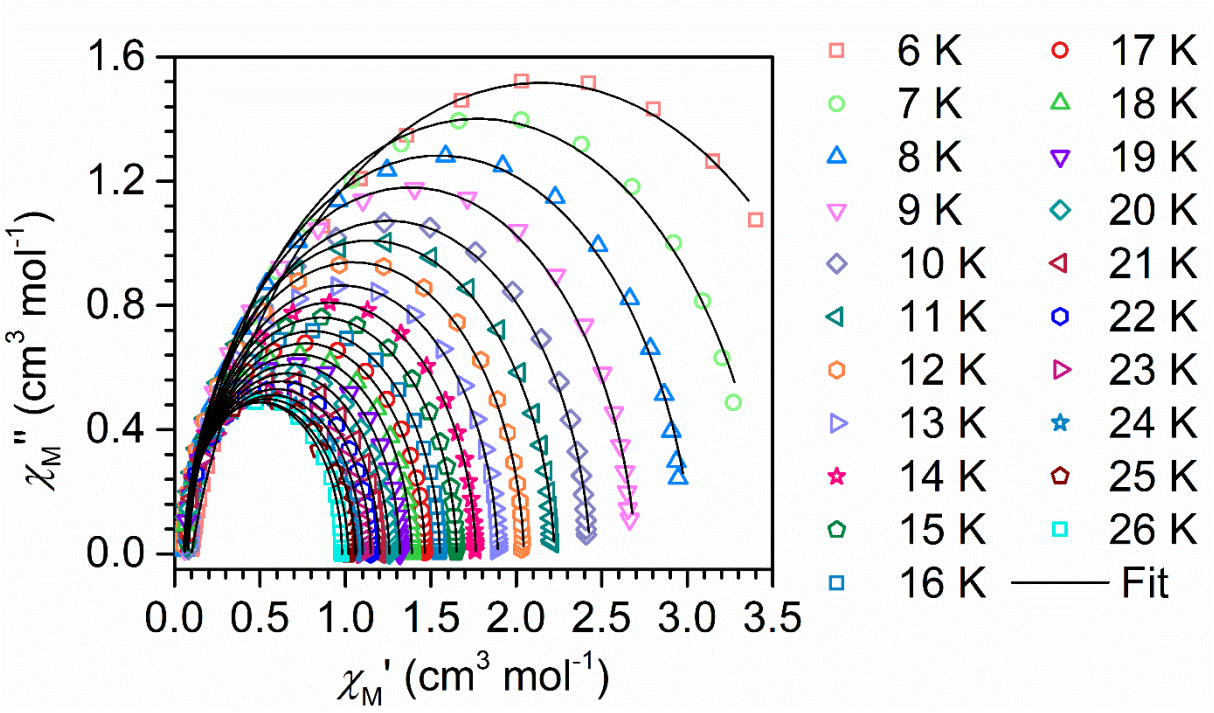

Figure S14. Cole-Cole (Argand) plots for ac susceptibility collected from 6 to 26 K under 0 Oe applied dc field for **3**. Symbols represent the experimental data points and the points representing the fits are connected by black solid lines, representing fits to a generalized Debye model.

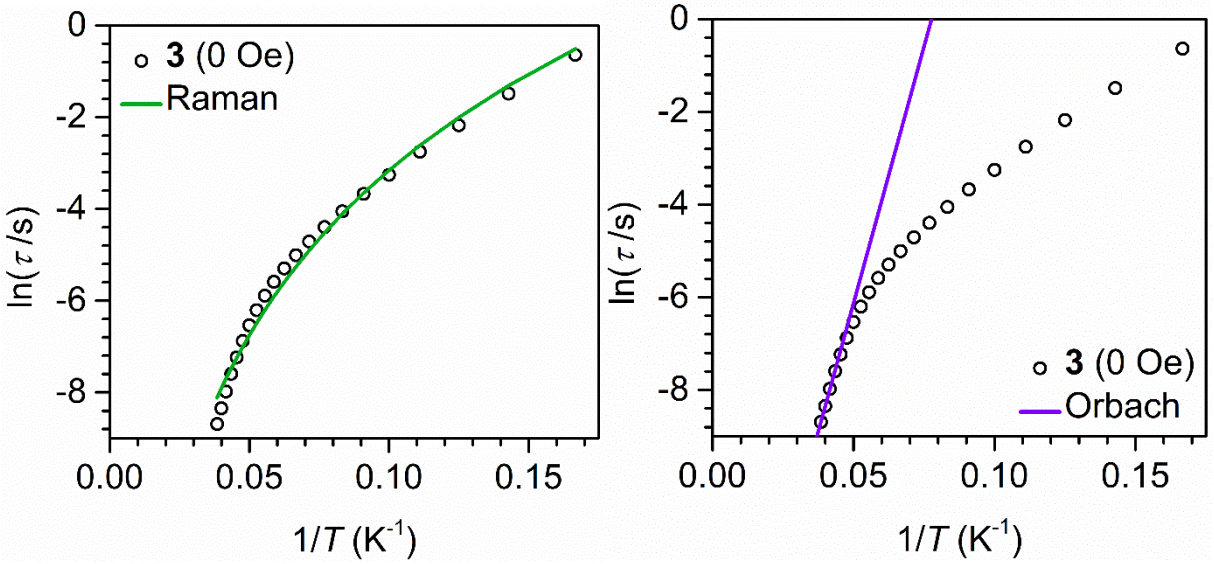

Figure S15. Arrhenius plots (ln(τ) vs. 1/*T*) derived from ac magnetic susceptibility measurements between 6 and 26 K under a 0 Oe applied dc field for [(Cp*$_2$Dy)$_2$(μ-bim)] (**3**), including a fit to a single Raman process (left, green line) and an Orbach fit to the three highest T data points (right, violet line). Fit values: C = 1.6(2) × 10^{-4} s^{-1} K^{-n}, n = 5.18(2) (left), U_{eff} = 153.9(5) cm^{-1}, τ_0 = 3.31(8) × 10^{-8} s.

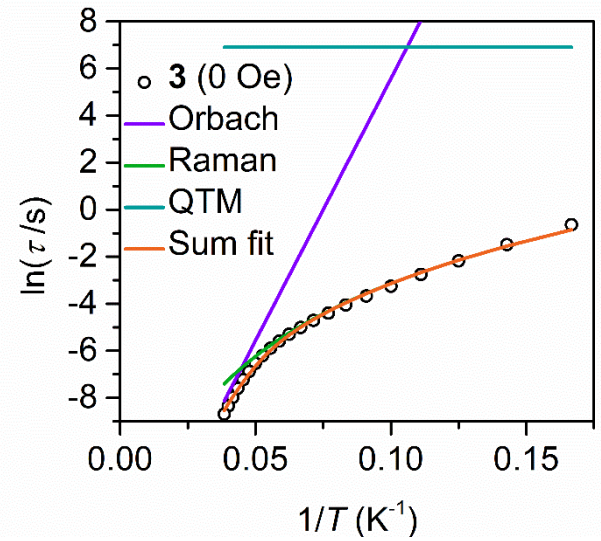

Figure S16. Arrhenius plot derived from ac magnetic susceptibility measurements between 6 and 26 K under a 0 Oe applied dc field for [(Cp*$_2$Dy)$_2$(μ-bim)] (**3**), including a fit to a sum of Orbach, Raman and QTM processes (red line). Orbach, Raman and QTM contributions are depicted as purple, green und cyan lines, respectively. Fit values: U_{eff} = 159(1) cm^{-1}, τ_0 = 5.2(1) × 10^{-8} s, τ_{QTM} = 20.68(2) s, C = 2.1(1) × 10^{-4} s^{-1} K^{-n}, n = 4.9(1).

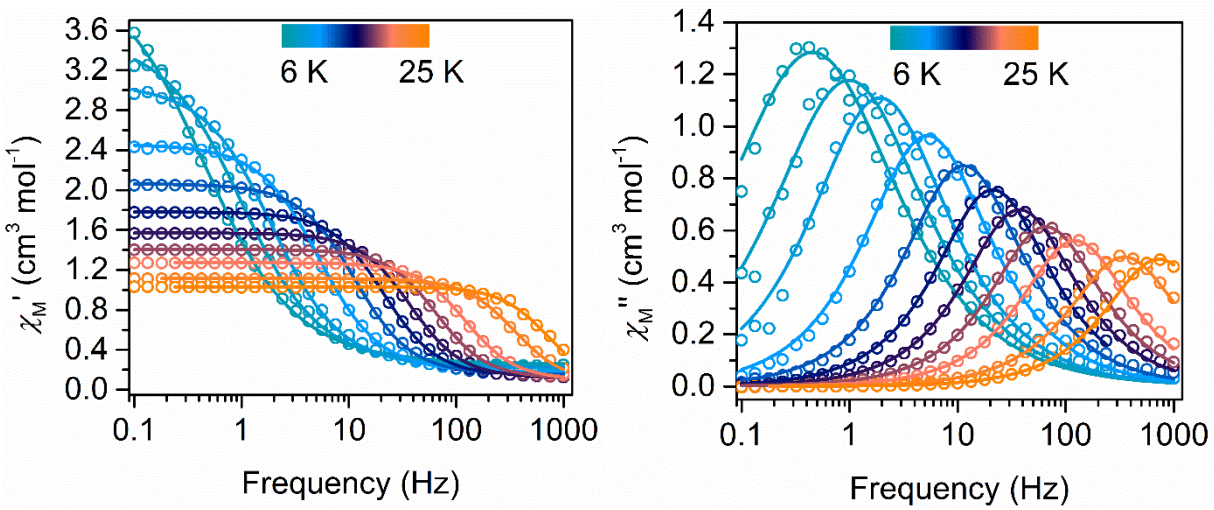

Figure S17. Variable-temperature, variable-frequency in-phase (χ_M') (left) and out-of-phase (χ_M'') (right) ac magnetic susceptibility data collected for **3** under a 2000 Oe applied dc field from 2 to 25 K. Solid lines represent fits to the data between 6 and 26 K,

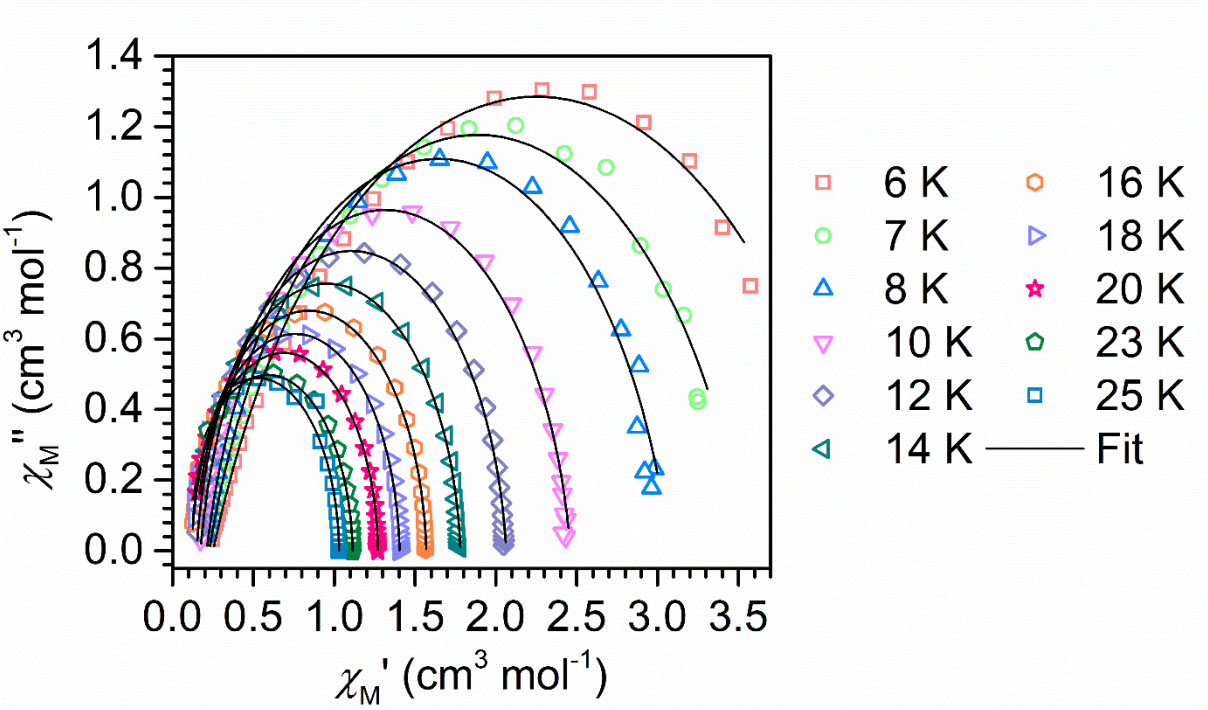

Figure S18. Cole-Cole (Argand) plots for ac susceptibility collected from 6 to 25 K under 2000 Oe applied dc field for **3**. Symbols represent the experimental data points and the points representing the fits are connected by black solid lines, representing fits to a generalized Debye model.

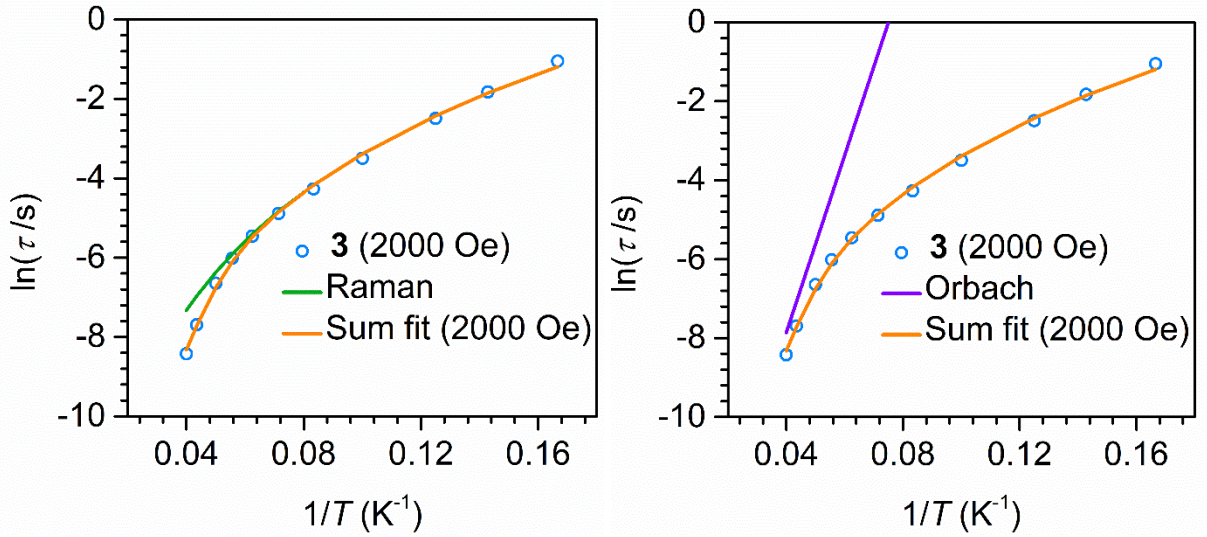

Figure S19. Arrhenius plots (ln(τ) vs. 1/*T*) derived from ac magnetic susceptibility measurements between 6 to 25 K under a 2000 Oe applied dc field (blue circles) for [(Cp*$_2$Dy)$_2$(μ-bim)] (**3**), including a sum fit to a Raman and Orbach process (orange line) with individual Raman (left, green line) and Orbach (right, purple line) contributions. Fit values: C = 1.5(2) × 10^{-3} s^{-1} K^{-n}, n = 4.30(1) (left), U_{eff} = 156(1) cm^{-1}, τ_0 = 4.8(1) × 10^{-8} s.

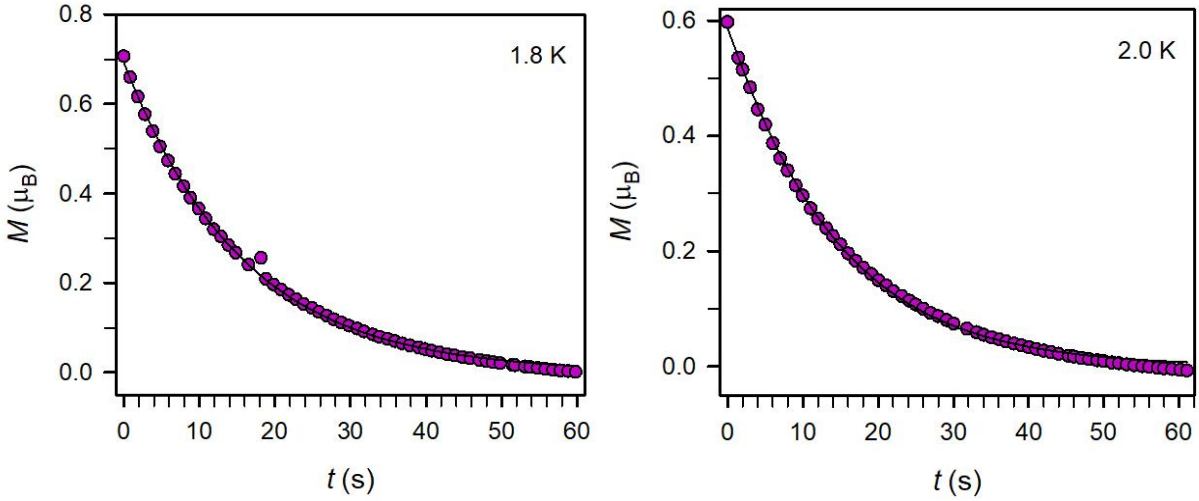

Figure S20. Plots of magnetization vs. time used to derive relaxation times for **3** at 1.8 K (left) and 2.0 K (right). The data (purple circles) were fit using a stretched exponential function y = a · exp (−((t/τ)b)). The magnetization data were obtained by applying a magnetic field of 7 T to the sample at temperatures of 1.8 and 2.0 K for 5 min, and then removing the external magnetic field.

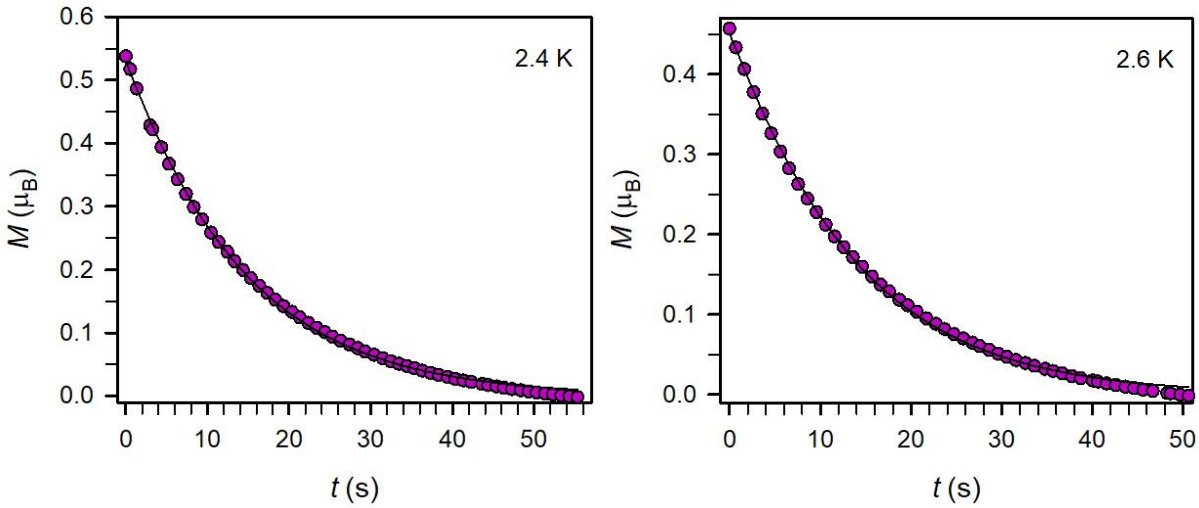

Figure S21. Plots of magnetization vs. time used to derive relaxation times for **3** at 2.4 K (left) and 2.6 K (right). The data (purple circles) were fit using a stretched exponential function y = a · exp (−((t/τ)b)). The magnetization data were obtained by applying a magnetic field of 7 T to the sample at temperatures of 2.4 K and 2.6 K for 5 min, and then removing the external magnetic field.

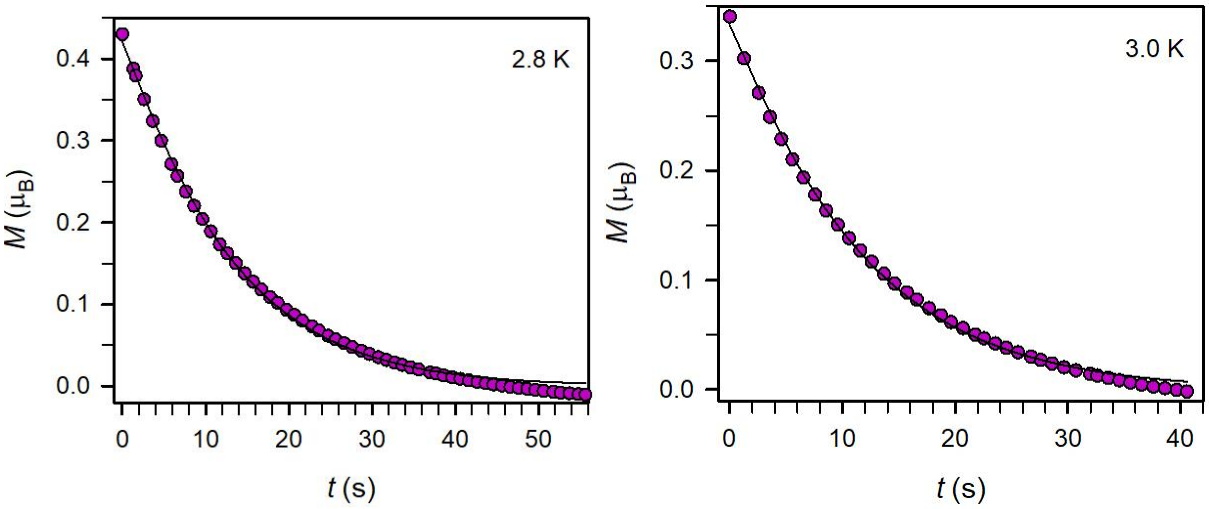

Figure S22. Plots of magnetization vs. time used to derive relaxation times for **3** at 2.8 K (left) and 3.0 K (right). The data (purple circles) were fit using a stretched exponential function y = a · exp (−((t/τ)b)). The magnetization data were obtained by applying a magnetic field of 7 T to the sample at temperatures of 2.8 K and 3.0 K for 5 min, and then removing the external magnetic field.

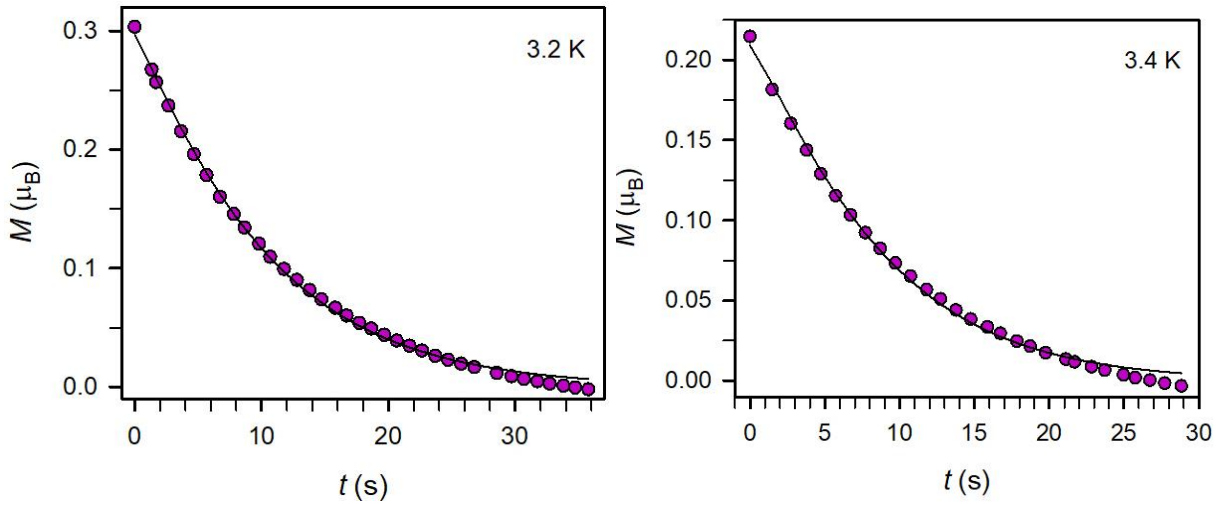

Figure S23. Plots of magnetization vs. time used to derive relaxation times for **3** at 3.2 K (left) and 3.4 K (right). The data (purple circles) were fit using a stretched exponential function y = a · exp (−((t/τ)b)). The magnetization data were obtained by applying a magnetic field of 7 T to the sample at temperatures of 3.2 K and 3.4 K for 5 min, and then removing the external magnetic field.

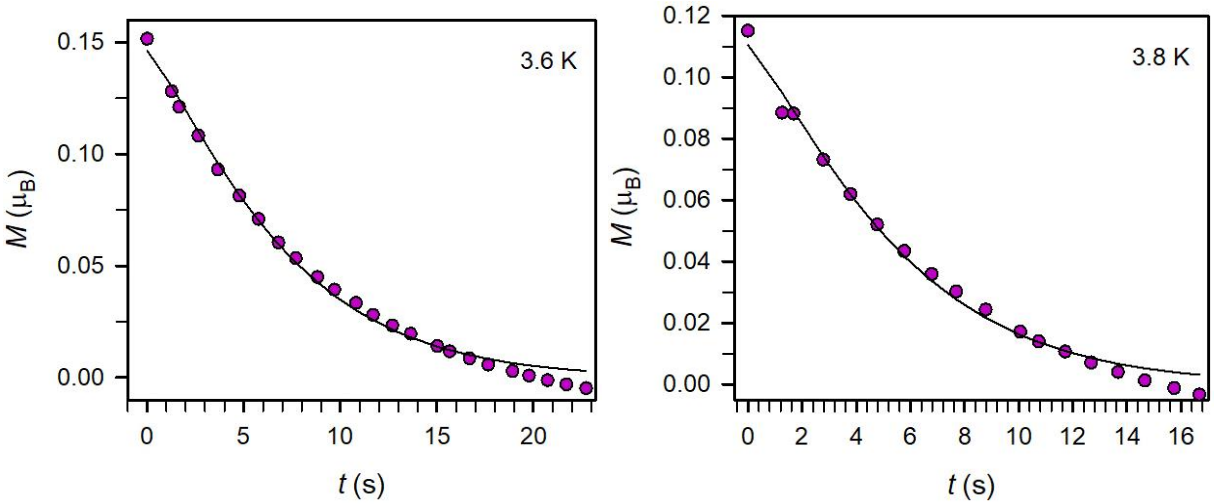

Figure S24. Plots of magnetization vs. time used to derive relaxation times for **3** at 3.6 K (left) and 3.8 K (right). The data (purple circles) were fit using a stretched exponential function y = a · exp (−((t/τ)b)). The magnetization data were obtained by applying a magnetic field of 7 T to the sample at temperatures of 3.6 K and 3.8 K for 5 min, and then removing the external magnetic field.

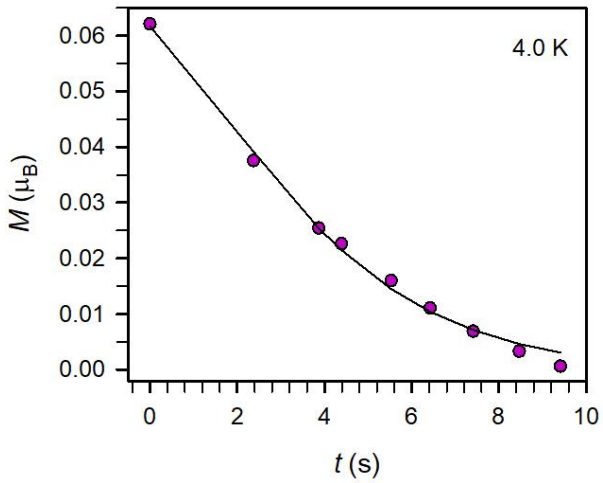

Figure S25. Plot of the normalized magnetization decay curves used to derive relaxation times for **3** at 4.0 K. The data (purple circles) were fit using a stretched exponential function y = a · exp (−((t/τ)b)). The magnetization data were obtained by applying a magnetic field of 7 T to the sample at temperature of 4.0 K for 5 min, and then removing the external magnetic field.

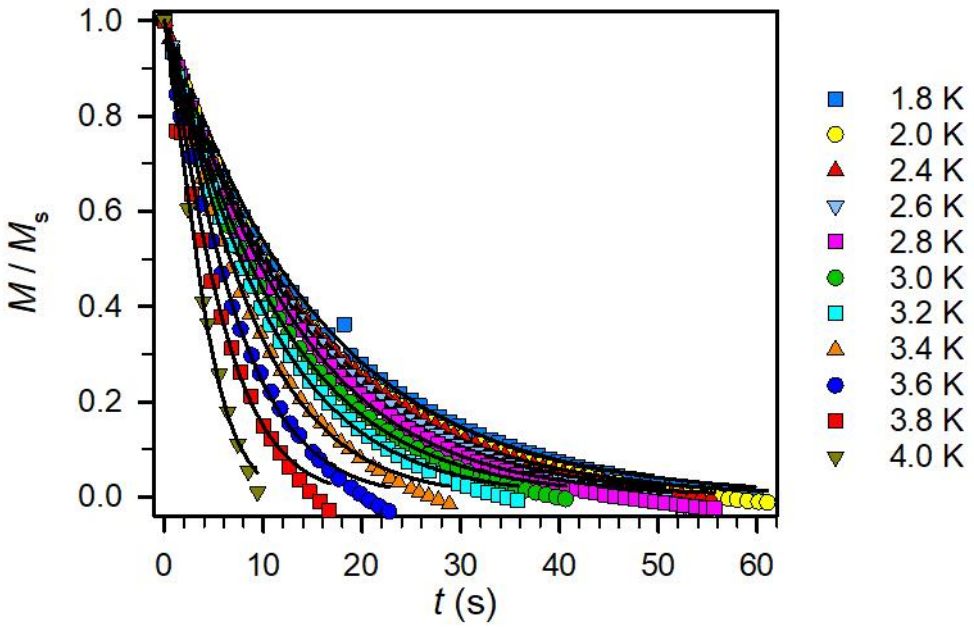

Figure S26. Plots of magnetization vs. time used to derive relaxation times for **3** between 1.8 K and 4.0 K. The data (purple circles) were fit using a stretched exponential function y = a · exp (−((t/τ)b)). The magnetization data were obtained by applying a magnetic field of 7 T to the sample at temperatures between 1.8 and 4.0 K for 5 min, and then removing the external magnetic field.

Table S9. Relaxation times, τ (s), and stretch factors, b, at various temperatures, T (K) for **3** used to fit dc relaxation measurements in Figure and Figure .

T (K)	τ (s)	Stretch factor
1.8	15.60688503	1.010445814
2.0	14.53420366	1.036308356
2.4	14.54687497	1.033730693
2.6	13.92974321	1.056526807
2.8	13.12726354	1.087532352
3.0	11.82225539	1.080314008
3.2	10.64462535	1.105142705
3.4	9.112171659	1.162860611
3.6	7.429914988	1.218015251
3.8	5.893699868	1.224121239
4.0	4.222034228	1.369707308

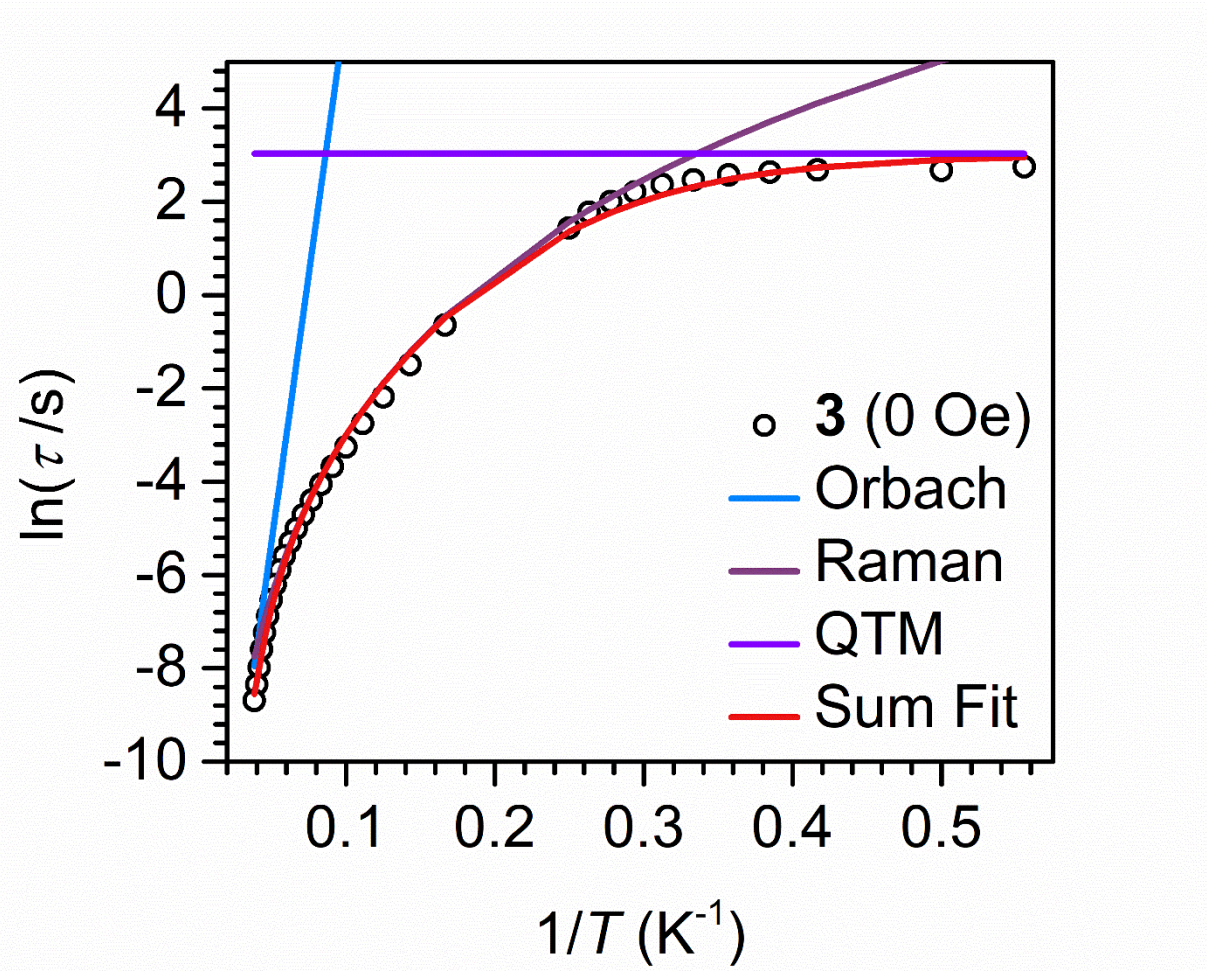

Figure S27. Arrhenius plot of relaxation time data derived from ac magnetic susceptibility measurements at temperatures from 6 to 26 K and dc relaxation experiments within the temperature range of 1.8 to 4 K (black circles) for **3**. The red solid line corresponds to a fit to one Orbach (blue solid line), one Raman (purple solid line) and one QTM (violet solid line) process. Relaxation times obtained from dc relaxation experiments are listed Table S9. Fit values: U_{eff} = 159(1) cm^{-1}, τ_0 = 5.2(1) × 10^{-8} s, τ_{QTM} = 20.68(2) s, C = 2.1(1) × 10^{-4}, n = 4.9(1).

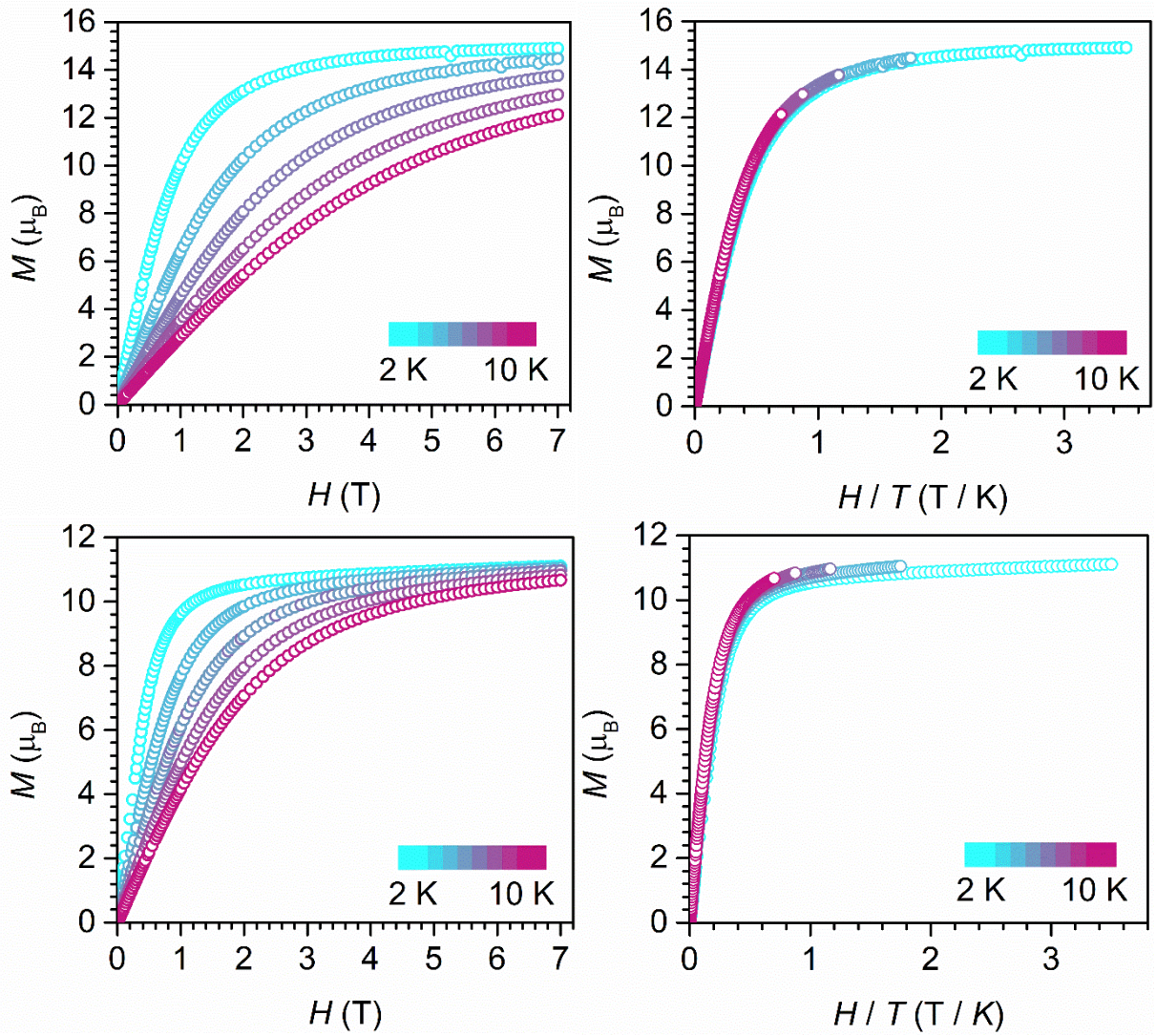

Figure S28. Variable temperature field-dependent magnetization curves recorded for [(Cp*$_2$Gd)$_2$(μ-bim)] (**2**, top left) and [(Cp*$_2$Dy)$_2$(μ-bim)] (**3**, bottom left) and reduced magnetization for **2** (top right) and **3** (bottom right). Measurements were carried out between 0 and 7 T at 2, 4, 6, 8 and 10 K.

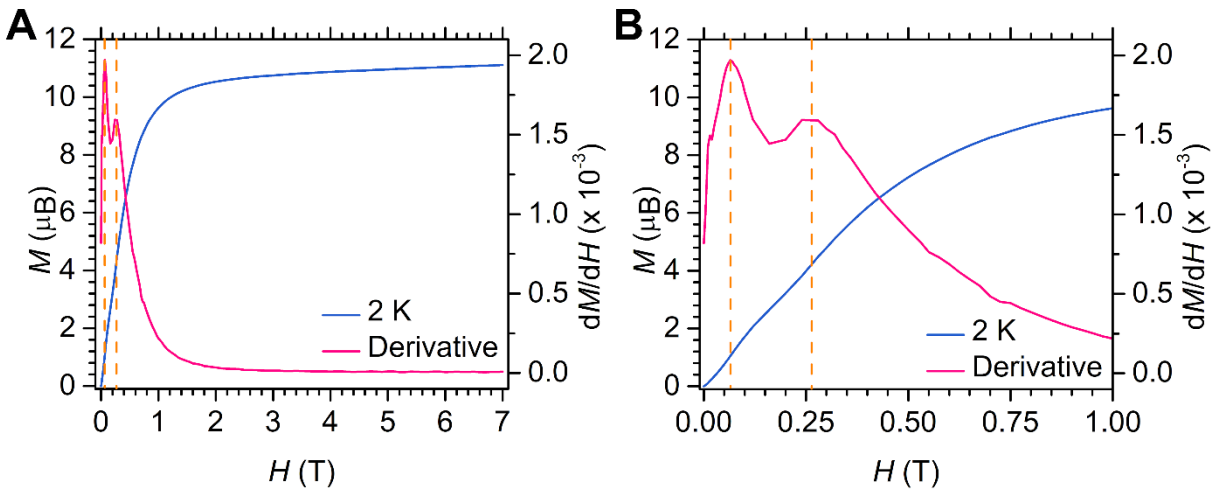

Figure S29. Variable temperature, field-dependent magnetization curves for [(Cp*$_2$Dy)$_2$(μ-bim)] (**3**) collected at 2 K and first derivative of the magnetization vs. applied magnetic field as the full (**A**) and magnified low field regime (**B**).

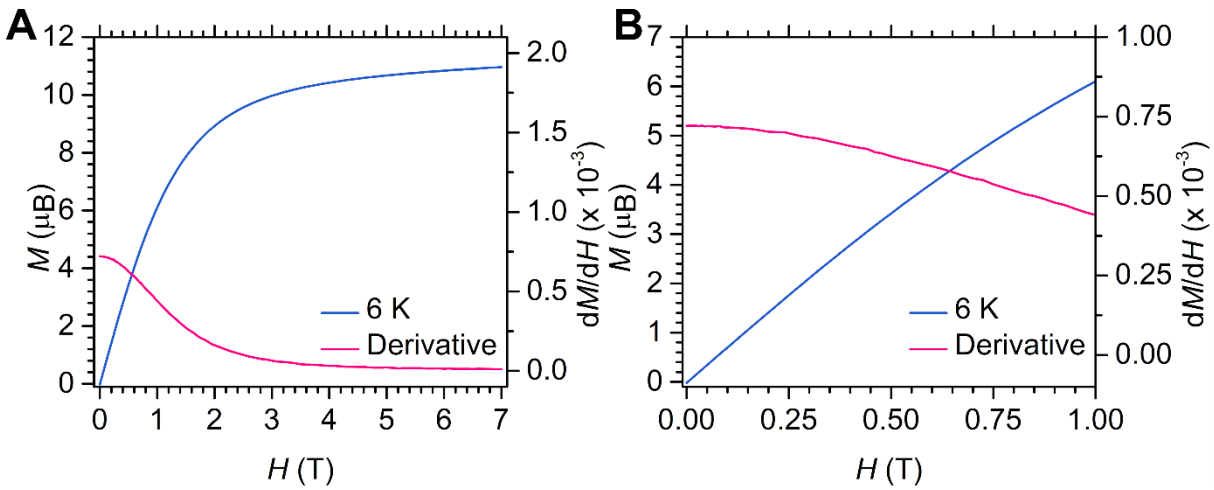

Figure S30. Variable temperature field-dependent magnetization curves for [(Cp*$_2$Dy)$_2$(μ-bim)] (**3**) collected at 6 K and first derivative of the magnetization vs. applied magnetic field as the full (**A**) and magnified low field regime (**B**).

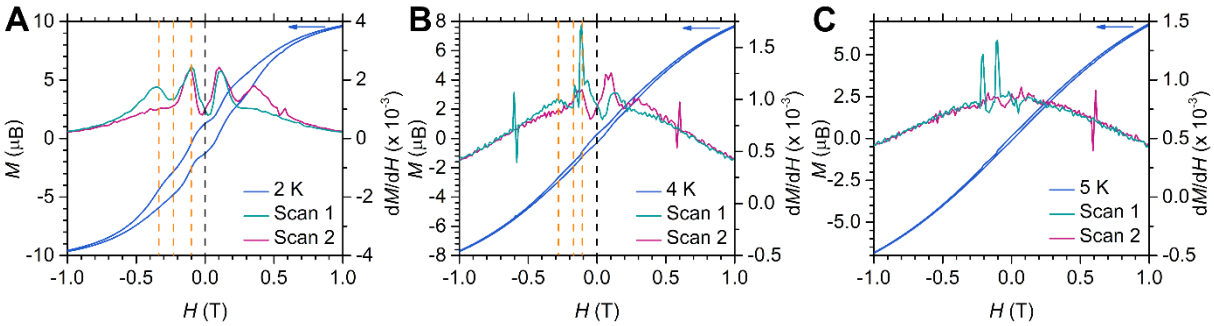

Figure S31. Isothermal variable-field magnetization (*M*) data of [(Cp*$_2$Dy)$_2$(μ-bim)] (**3**) collected at 2 K (**A**), 4 K (**B**) and 5 K (**C**) with an average sweep rate of 0.01 T s^{-1} (blue lines). The first derivatives d*M*/d*H* vs *H* are plotted color-coded, where green lines represent the scan from +7 T → −7 T (scan 1), and purple lines represent the −7 T → +7 T scans (scan 2). The features in the derivative spectra at ~ ±0.5 T in **A** and ~ ±0.6 T in **B** and **C** are artifacts, likely arising from noise due to the VSM measurement mode of the magnetometer operative during the measurement.

10 References

1 S. Demir, J. M. Zadrozny, M. Nippe and J. R. Long, Exchange Coupling and Magnetic Blocking in Bipyrimidyl Radical-Bridged Dilanthanide Complexes, *J. Am. Chem. Soc.*, 2012, **134**, 18546–18549.

2 B. F. Fieselmann, D. N. Hendrickson and G. D. Stucky, Synthesis, Electron Paramagnetic Resonance, and Magnetic Studies of Binuclear Bis(η^5-cyclopentadienyl)titanium(III) Compounds with Bridging Pyrazolate, Biimidazolate, and Bibenzimidazolate Anions, *Inorg. Chem.*, 1978, **17**, 2078–2084.

3 G. A. Bain and J. F. Berry, Diamagnetic Corrections and Pascal's Constants, *J. Chem. Edu.*, 2008, **85**, 532–536.

4 *COSMO V1.61, Software for the CCD Detector Systems for Determining Data Collection Parameters*, Bruker Analytical X-ray Systems, Madison, WI, 2009.

5 *APEX2 V2010.11-3, Software for the CCD Detector System*, Bruker Analytical X-ray Systems, Madison, WI, 2010.

6 R. H. Blessing, *SAINT V 7.68a, Software for the Integration of CCD Detector System*, Bruker Analytical X-ray Systems, Madison, WI, 2010.

7 R. H. Blessing, SADABS V2.008/2, Program for Absorption Corrections using Bruker-AXS CCD, *Acta Cryst.* 1995, **A51**, 33-38.

8 O. V. Dolomanov, L. J. Bourhis, R. J. Gildea, J. A. K. Howard and H. Puschmann, OLEX2: A Complete Structure Solution, Refinement and Analysis Program, *J. Appl. Crystallogr.*, 2009, **42**, 339–341.

9 G. M. Sheldrick, SHELXT - Integrated Space-Group and Crystal-Structure Determination, *Acta Cryst.*, 2015, **A71**, 3–8.

10 G. M. Sheldrick, Crystal Structure Refinement with SHELXL, *Acta Cryst.*, 2015, **C71**, 3–8.

11 G. M. Sheldrick, A Short History of ShelX, *Acta Cryst.*, 2008, **A64**, 112–122.

12 *CrysAlisPro Software System*, Rigaku Corporation, Oxford, 2020.

13 *SCALE3 ABSPACK, Empirical Absorption Correction, CrysAlis Pro - Software Package*, Rigaku Corporation, Oxford, 2020.

14 F. Neese, Software Update: The Orca Program System—Version 5.0, *Wiley Interdiscip. Rev. Comput. Mol. Sci.*, 2022, **12**, 1–15.

15 W. Humphrey, A. Dalke and K. Schulten, VMD - Visual Molecular Dynamics*, J. Molec. Graph.*, 1996, **14**, 33–38.

16 V. N. Staroverov, G. E. Scuseria, J. Tao and J. P. Perdew, Erratum: Comparative Assessment of a new Nonempirical Density Functional: Molecules and Hydrogen-Bonded Complexes [J. Chem. Phys. 119, 12129 (2003)], *J. Chem. Phys.*, 2004, **121**, 11507.

17 F. Weigend and R. Ahlrichs, Balanced Basis Sets of Split Valence, Triple Zeta Valence and Quadruple Zeta Valence Quality for H to Rn: Design and Assessment of Accuracy, *Phys. Chem. Chem. Phys.*, 2005, **7**, 3297.

18 M. Dolg, H. Stoll and H. Preuss, Energy-Adjusted Ab Initio Pseudopotentials for the Rare Earth Elements, *J. Chem. Phys.*, 1989, **90**, 1730–1734.

19 F. Weigend, Accurate Coulomb-Fitting Basis Sets for H to Rn, *Phys. Chem. Chem. Phys.*, 2006, **8**, 1057.

20 S. Grimme, S. Ehrlich and L. Goerigk, Effect of the damping function in dispersion corrected density functional theory, *J. Comput. Chem.*, 2011, **32**, 1456–1465.

21 S. Grimme, J. Antony, S. Ehrlich and H. Krieg, A Consistent and Accurate Ab -initio Parametrization of Density Functional Dispersion Correction (DFT-D) for the 94 elements H-Pu, *J. Chem. Phys.*, 2010, **132**, 154104.

22 R. Izsák and F. Neese, An overlap fitted chain of spheres exchange method, *J. Chem. Phys.*, 2011, **135**, 144105.

23 F. Neese, F. Wennmohs, A. Hansen and U. Becker, Efficient, Approximate and Parallel Hartree–Fock and Hybrid DFT Calculations. A 'Chain-of-Spheres' Algorithm for the Hartree–Fock Exchange, *Chem. Phys.*, 2009, **356**, 98.

24 A. V. Marenich, C. J. Cramer and D. G. Truhlar, Universal Solvation Model Based on Solute Electron Density and on a Continuum Model of the Solvent Defined by the Bulk Dielectric Constant and Atomic Surface Tensions, *J. Phys. Chem. B*, 2009, **113**, 6378–6396.